Time-dependent models of accretion discs formed from compact object mergers

B. D. Metzger,[★] A. L. Piro and E. Quataert

Astronomy Department and Theoretical Astrophysics Center, University of California, Berkeley, 601 Campbell Hall, Berkeley, CA 94720, USA

ABSTRACT

We present time-dependent models of the remnant accretion discs created during compact object mergers, focusing on the energy available from accretion at late times and the composition of the disc and its outflows. We calculate the dynamics near the outer edge of the disc, which contains the majority of the disc's mass and determines the accretion rate on to the central black hole. This treatment allows us to follow the evolution over much longer time-scales (100 s or longer) than current hydrodynamic simulations. At late times the disc becomes advective and its properties asymptote to self-similar solutions with an accretion rate $\dot{M}_d \propto t^{-4/3}$ (neglecting outflows). This late-time accretion can in principle provide sufficient energy to power the late-time activity observed by *Swift* from some short-duration gamma-ray bursts. However, because outflows during the advective phase unbind the majority of the remaining mass, it is difficult for the remnant disc alone to produce significant accretion power well beyond the onset of the advective phase. Unless the viscosity is quite low ($\alpha \lesssim 10^{-3}$), this occurs before the start of observed flaring at $\sim$30 s; continued mass inflow at late times thus appears required to explain the late-time activity from short-duration gamma-ray bursts. We show that the composition of the disc freezes-out when the disc is relatively neutron rich (electron fraction $Y_e \simeq 0.3$). Roughly $10^{-2} M_\odot$ of this neutron-rich material is ejected by winds at late times. During earlier, neutrino-cooled phases of accretion, neutrino irradiation of the disc produces a wind with $Y_e \simeq 0.5$, which synthesizes at most $\sim$10$^{-3} M_\odot$ of ^{56}Ni. We highlight what conditions are favorable for ^{56}Ni production and predict, in the best cases, optical and infrared transients peaking $\sim$0.5–2 d after the burst, with fluxes a factor of $\sim$10 below the current observational limits.

Key words: accretion, accretion discs – black hole physics – neutrinos – gamma-rays: bursts.

1 INTRODUCTION

The most popular model for the creation of short-duration gamma-ray bursts (GRBs) is either binary neutron star (NS/NS) or black hole–neutron star (BH/NS) coalescence (Paczyński 1986, 1991; Eichler et al. 1989; Narayan, Piran & Shemi 1991). Support for the merger hypothesis comes from their durations of $\lesssim$2 s, observations of well-localized short GRBs in galaxies without strong star formation (Berger et al. 2005; Gehrels et al. 2005; Hjorth et al. 2005), and the lack of a detectable coincident supernovae (Hjorth et al. 2005; Bloom et al. 2006; Soderberg et al. 2006; Ferrero et al. 2007), as is found in the case of long ($\gtrsim$2 s) GRBs (Galama et al. 1998; Hjorth et al. 2003; Stanek et al. 2003).

Previous theoretical studies of the merger process have focused on one of two stages. The first is the *dynamical* portion in which the

less massive companion is tidally disrupted by the more massive BH (Lee & Kluźniak 1995, 1998, 1999; Kluźniak & Lee 1998; Janka et al. 1999; Rosswog, Speith & Wynn 2004) or NS (Ruffert, Janka & Schäfer 1996; Ruffert & Janka 1999; Oechslin & Janka 2006). The details of whether a dynamical instability (Lai, Rasio & Shapiro 1994; Rasio & Shapiro 1994) or Roche lobe overflow occurs depends on the mass ratio and the nuclear equation of state (EOS; Bildsten & Cutler 1992; Uryū & Eriguchi 1999).

Nevertheless, generally $\sim$0.01–0.1 $M_\odot$ of material remains in a remnant disc following the dynamical stage. The accretion of this material on to the central object gives rise to the second, *disc* portion of the merger. The energetics and time-scale of the accretion phase are reasonably consistent with observations of short GRBs, as was shown by models of steady-state, azimuthally symmetric, vertically averaged discs (Popham, Woosley & Fryer 1999; Narayan, Piran & Kumar 2001; DiMatteo, Perna & Narayan 2002; Kohri & Mineshige 2002; Chen & Beloborodov 2007). More recently, these discs have been modelled with time-dependent calculations in

★E-mail: bmetzger@astro.berkeley.edu

one-dimensional (1D; Janiuk et al. 2004), two-dimensional (2D; Lee, Ramirez-Ruiz & Page 2004, 2005) and three-dimensional (3D; Setiawan, Ruffert & Janka 2004, 2006). The typical time interval that present multidimensional calculations can simulate is on the order of the burst duration or less (~1–2 s for 2D and ~50 ms for 3D).

Recent observations of short GRBs by *Swift*, however, indicate continued activity from the central engine on much longer time-scales. X-ray flares with durations of ~100 s after a delay of ~30 s have been seen from several bursts (Barthelmy et al. 2005; Villasenor et al. 2005; La Parola et al. 2006; Campana et al. 2006). Stacked light curves of many bursts indicate continued activity on a similar time-scale (Lazzati, Ramirez-Ruiz & Ghisellini 2001; Montanari et al. 2005). In one extreme case, GRB 050724 displayed an X-ray flare 12 h post-burst. This flaring activity has been attributed to a number of different sources, including fragmentation of a rapidly rotating core (King et al. 2005), magnetic regulation of the accretion flow (Proga & Zhang 2006), fragmentation of the accretion disc (Perna, Armitage & Zhang 2005; although this explanation may have difficulty reproducing the observed time-scales, Piro & Pfahl 2007), differential rotation in a post-merger millisecond pulsar (Dai et al. 2006) and an infalling tidal tail of material stripped from the disrupted NS (Lee & Ramirez-Ruiz 2007; Rosswog 2007).

In order to determine whether the late-time activity from short GRBs is consistent with a compact merger origin, the disc evolution should be followed for time-scales much longer than the initial viscous time. With this aim, we perform time-dependent calculations modelling the disc as an annulus that contains the majority of the mass. This simplification allows us to study the disc evolution for arbitrarily long time-scales, and to readily determine important properties such as the disc's composition and when it becomes advective. We are also able to survey much of the parameter space of initial disc mass and angular momentum. In Section 2 we discuss the initial conditions for discs formed from compact object mergers. This is followed by Section 3, in which we summarize the main assumptions of our ring model. In Section 4 we present the results of our calculations and summarize the main properties of the models. We then calculate outflows from our disc solutions in Section 5. We investigate the composition of the outflows and argue that they generally consist of neutron-rich isotopes, but can produce ^{56}Ni in some circumstances. The presence or lack of an optical transient from short GRBs therefore provides an important constraint on progenitor models. We conclude in Section 6 with a discussion of our results. In Appendix A we summarize the Green's function solution to the viscous spreading of a ring, which is important for connecting our ring model to the true extended disc geometry. In Appendix B we present analytic self-similar solutions that reproduce many of the features of our numerical solutions.

2 INITIAL CONDITIONS

The dynamical phase of NS/NS or BH/NS mergers has been studied extensively using a number of different numerical techniques and methods for including general relativity (GR). Here we summarize some of the most relevant features for our study (for a more detailed review, see Lee & Ramirez-Ruiz 2007).

When the lighter companion NS is first tidally disrupted, a debris disc is formed within only a few dynamical time-scales. The initial disc mass, $M_{d,0}$, is generally larger for more asymmetric mass ratios (i.e. small q, where q is the ratio of the lighter to the heavier binary component). For example, Shibata & Taniguchi (2006) find that for

a NS/NS merger with $q = 0.7$ that $M_{d,0} = 0.03\,M_\odot$, but for $q = 0.9$ the disc is much less massive with $M_{d,0} = 10^{-3}\,M_\odot$. Another trend is that including strong gravity gives less massive remnant discs. The BH spin is also important, with larger spin favoring disc formation (Rasio et al. 2005) and the production of a tidal tail. These have masses of $\simeq 0.01$–$0.05\,M_\odot$ and may provide prolonged mass inflow (Lee & Ramirez-Ruiz 2007), but for simplicity this will be ignored here. Taken together, these simulations generally find $M_{d,0} \simeq 0.01$–$0.3\,M_\odot$, with the disc containing a substantial fraction of the angular momentum of the disrupted companion.

In the standard picture of NS–NS mergers, the resulting hypermassive NS collapses to a BH shortly following the merger. However, simulations show that when (and if) collapse actually occurs depends on the mass of the central NS and its ability to transport angular momentum to the surrounding disc (Shibata, Taniguchi & Uryū 2005; Shibata & Taniguchi 2006; Shibata et al. 2006). In fact, if the NS remains supported by differential rotaton for several seconds (Baumgarte, Shapiro & Shibata 2000; Duez et al. 2004, 2006; Morrison, Baumgarte & Shapiro 2004) or loses sufficient mass via a centrifugally driven outflow (e.g. Thompson, Chang & Quataert 2004; Dessart et al. 2008a), the NS itself may power the GRB (e.g. Price & Rosswog 2006). In this paper we assume that the central object promptly collapses to a BH; our model, however, would be reasonably applicable for the case of a central NS as well, the primary difference being that the significant neutrino flux from the newly formed NS and from the boundary layer between the disc and the NS could modify the composition and thermal properties of the disc.

We present some characteristic numbers to motivate our choice of initial conditions. Consider a binary with masses M and m ($M > m$), where the latter is the NS (with radius R) that is tidally disrupted. The disruption radius, a_t, is estimated to be (Kopal 1959, adding Fishbone's 1973 10 per cent strong gravity correction)

$$a_t \simeq 2.4R \left(\frac{M+m}{m} \right)^{1/3}. \tag{1}$$

The characteristic orbital period at this radius is

$$P_t \simeq 23.4 \left(\frac{R^3}{Gm} \right)^{1/2} \simeq 2 \times 10^{-3} m_{1.4}^{-1/2} R_6^{3/2}\,\text{s}, \tag{2}$$

where $m_{1.4} = m/1.4\,M_\odot$ and $R_6 = R/10^6$ cm, with an orbital angular momentum of

$$\begin{aligned} J_t &= [G(M+m)a_t]^{1/2}\,m \\ &\simeq 6 \times 10^{49} (1/q+1)^{2/3} m_{1.4}^{3/2} R_6^{1/2}\,\text{erg s}, \end{aligned} \tag{3}$$

where $q = m/M$. The disrupted NS also contains spin angular momentum. This is negligible since the NS is not strongly affected by tidal coupling (Bildsten & Cutler 1992). Even a rapidly rotating NS ($\simeq 5$ ms) has an associated angular momentum of merely $\sim 10^{48}$ erg s.

Once disrupted, a considerable fraction of the NS is either lost from the system or immediately swallowed by the BH. The remaining material forms a thick torus surrounding the central BH. Its associated viscous time-scale can be estimated by assuming that the majority of the torus' mass lies at a single radius, $r_{d,0}$. Taking the angular momentum of the disc to be $J_d \simeq (GMr_{d,0})^{1/2} M_{d,0}$, we estimate

$$r_{d,0} \simeq 3 \times 10^7 M_3^{-1} M_{0.1}^{-2} \left(\frac{J_{49}}{2} \right)^2\,\text{cm}, \tag{4}$$

where $M_3 = M/3\,M_\odot$, $M_{0.1} = M_{d,0}/0.1\,M_\odot$ and $J_{49} = J_d/10^{49}$ erg s. For a disc with half-thickness H, the viscous

time-scale is

$$
t_{\mathrm{visc},0} = \alpha^{-1} \left(\frac{r_{\mathrm{d}}}{H} \right)^2 \left(\frac{r_{\mathrm{d}}^3}{GM} \right)^{1/2}
$$

$$
\simeq 6 \times 10^{-2} \alpha_{0.1}^{-1} M_3^{-1/2} r_7^{3/2} \left(\frac{H}{0.5 r_{\mathrm{d}}} \right)^{-2} \mathrm{s}, \tag{5}
$$

where $\alpha = 0.1\alpha_{0.1}$ is the standard dimensionless viscosity (Shakura & Sunyaev 1973), $r_7 = r_{\mathrm{d},0}/10^7$ cm, and we have scaled to an initial ratio of $H/r_{\mathrm{d}} = 0.5$, consistent with our numerical solutions. The initial viscous time $t_{\mathrm{visc},0}$ is roughly the time at which the central BH begins accreting in earnest. The strong dependence of $t_{\mathrm{visc},0}$ on disc mass and radius demonstrates that the initial evolution of the disc is sensitive to the outcome of the dynamical phase of the merger. But as we will show, the late time evolution is much less sensitive to initial conditions and is well described by self-similar solutions.

3 PHYSICS OF THE EXPANDING RING MODEL

Given these initial conditions, one would like to know how the disc then evolves. Modelling the entire disc requires resolving time-scales over ~4–6 orders of magnitude. This makes it expensive to carry out simulations for long periods of time. We consider instead a simplified model that captures most of the features of interest. At any given time, t, the disc can be broken into three regions depending on the local viscous time, t_{visc}, which increases with radius, roughly as $t_{\mathrm{visc}} \sim r^{3/2}$. At small radii, $t_{\mathrm{visc}} < t$, and the disc comes into steady state. This is the region most often modelled in previous studies (Popham et al. 1999; Narayan et al. 2001; DiMatteo et al. 2002; Kohri & Mineshige 2002; Chen & Beloborodov 2007). The radii where $t_{\mathrm{visc}} \sim t$ contain the majority of the disc's mass and angular momentum. Therefore, this region determines the viscous evolution of the rest of the disc, including the mass accretion rate that is fed to the interior steady-state region. Motivated by this fact, we focus on this radius and model the disc as a ring. Exterior to this point is a third region where $t_{\mathrm{visc}} > t$, but this contains a small amount of mass and is negligible for the viscous evolution.

3.1 Dynamical equations

Our ring model treats the disc as a single annulus that is evolved forward in time. In this picture, the properties of the ring, such as its surface density Σ and temperature T, are representative of the location where Σr^2 peaks. The main drawback of this method is that the material in the disc is in fact distributed spatially in radius. Thus, although the mass of the disc in the vicinity of r_{d} is $\simeq \pi \Sigma r_{\mathrm{d}}^2$, the total mass of the disc (integrated over all radii) is $M_{\mathrm{d}} = A\pi \Sigma r_{\mathrm{d}}^2$, where A is a factor of order unity that accounts for the distinction between the total mass of the disc and the mass of the material near r_{d}. Similarly, we write the total angular momentum of the disc as $J_{\mathrm{d}} = B(GMr_{\mathrm{d}})^{1/2} \pi r_{\mathrm{d}}^2 \Sigma$. At early times the constants A and B depend on the initial conditions of how matter is spatially distributed; however, at times much greater than the initial viscous time (given by equation 5), material initially concentrated at a given radius becomes spread out in a manner determined by the viscosity. As described in detail in Appendix A, we choose the constants A and B by setting the solution of our simplified ring model at late times equal to the Green's function solution for a spreading ring with a viscosity $\nu \propto r^{1/2}$ (as is appropriate for the radiatively inefficient

disc at late times). This fixes $A = 3.62$ and $B = 3.24$.[1] Conveniently $A/B \simeq 1$, so that it is a good approximation to take $J_{\mathrm{d}} \simeq (GMr_{\mathrm{d}})^{1/2} M_{\mathrm{d}}$.

The time evolution of the disc is determined by the conservation equations. Conservation of mass is

$$
\frac{\mathrm{d}}{\mathrm{d}t} \left(A\pi \Sigma r_{\mathrm{d}}^2 \right) = -\dot{M}_{\mathrm{d}}, \tag{6}
$$

where $\dot{M}_{\mathrm{d}}$ is in general the total mass-loss rate, which could include both accretion and a wind (for now we ignore the effects of a wind). Conservation of angular momentum is

$$
\frac{\mathrm{d}}{\mathrm{d}t} \left[B(GMr_{\mathrm{d}})^{1/2} \pi \Sigma r_{\mathrm{d}}^2 \right] = -\dot{J}, \tag{7}
$$

where $\dot{J}$ is the angular momentum loss rate. Equations (6) and (7) provide two coupled equations that can be solved for the dependent variables r_{d} and Σ.

The accretion rate must depend on the characteristic mass and viscous time-scale of the ring, so we use

$$
\dot{M}_{\mathrm{d}} = f M_{\mathrm{d}}/t_{\mathrm{visc}}, \tag{8}
$$

where $t_{\mathrm{visc}} = r_{\mathrm{d}}^2/\nu$ and ν is the viscosity. The factor f is set like A and B to match the exact solution of a spreading ring with $\nu \propto r^{1/2}$ (Appendix A), which gives $f = 1.6$.[2] Requiring a no-torque boundary condition at a radius r_*, we take

$$
f = 1.6 / \left[1 - (r_*/r_{\mathrm{d}})^{1/2} \right]. \tag{9}
$$

In contrast, a steady-state disc obeys $\dot{M}_{\mathrm{d}} = 3\pi\nu\Sigma$ (ignoring the no-torque condition), which instead gives $f = 3/A \simeq 0.83$.

For the viscosity, we use an α prescription:

$$
\nu = \alpha c_{\mathrm{s}} H, \tag{10}
$$

where $c_{\mathrm{s}} = (P/\rho)^{1/2}$ is the isothermal sound speed. The EOS includes contributions from radiation pressure, gas pressure, relativistic degeneracy pressure and neutrino pressure as in DiMatteo et al. (2002).

3.2 Energetics

For the energy equation, we take

$$
q_{\mathrm{visc}} = q_\nu^- + q_{\mathrm{adv}}, \tag{11}
$$

where q_{visc} is the viscous heating, q_ν^- is the neutrino cooling (using the prescriptions given by DiMatteo et al. 2002, which includes neutrino optical-depth effects), q_{adv} is the advective heat flux, and all q values correspond to half the disc thickness.

For a disc rotating at the Keplerian frequency $\Omega = (GM/r_{\mathrm{d}}^3)^{1/2}$,

$$
q_{\mathrm{visc}} = \frac{9}{8}\nu\Omega^2\Sigma = \frac{9}{8fA} \frac{GM\dot{M}_{\mathrm{d}}}{\pi r_{\mathrm{d}}^3} \left[1 - \left(\frac{r_*}{r_{\mathrm{d}}} \right)^{1/2} \right], \tag{12}
$$

where the prefactor $9/(8fA) \simeq 0.2$ is different from the steady-state value of $3/8$. The advective term, q_{adv}, is set as in DiMatteo et al. (2002), with the only difference being that the radial velocity is the expansion rate of the ring's radius:

$$
V_{\mathrm{r}} = \frac{\mathrm{d}r_{\mathrm{d}}}{\mathrm{d}t} = \frac{2\dot{M}}{A\pi r_{\mathrm{d}}\Sigma}, \tag{13}
$$

where we have taken $\dot{J} = 0$.

---

[1] In fact, when the total angular momentum is conserved, the viscous evolution is independent of A/B as long as A/B is nearly constant with time.
[2] Although we set $t_{\mathrm{visc}} = r^2/\nu$, any prefactors that could go into this prescription would just be absorbed into a redefinition of f.

Fusion to α particles produces heating in addition to $q_{\rm visc}$, with

$$q_{\rm nucl} = 6.8 \times 10^{28} \rho_{10} \frac{{\rm d}X_\alpha}{{\rm d}t} H, \tag{14}$$

where all quantities are expressed in cgs units, $\rho_{10} = \rho/10^{10} \, {\rm g \, cm^{-3}}$ and X_α is the mass fraction of α particles. Note that in our case $q_{\rm nucl} > 0$ since α particles are synthesized as the disc expands (in contrast to studies that follow cooling from photodisintegration as material moves inward). In our calculations we do not include $q_{\rm nucl}$ in solving equation (11) because we were not able to find reasonable solutions when doing so (for reasons explained in Section 4.1).

3.3 Composition

An advantage of the ring model is that other properties of the disc, such as its composition, can be cast into differential equations and integrated along with equations (6) and (7). Since the neutron content of the disc is particularly important for determining the properties of the disc's outflows, we evolve the electron fraction Y_e using

$$\frac{{\rm d}Y_e}{{\rm d}t} = -Y_e r_{e^-p} + (1 - Y_e) r_{e^+n}, \tag{15}$$

where $Y_e = X_p/(X_n + X_p)$, X_p and X_n are the proton and neutron mass fraction, respectively, and r_{e^-p} and r_{e^+n} are the electron and positron capture rates, respectively (Beloborodov 2003b). We have neglected the effect of neutrino absorptions on the evolution of Y_e in equation (15). Although absorptions are important at early times when the disc is optically thick, we are primarily concerned with the late-time value of Y_e, which does not depend sensitively on the neutrino irradiation (see Section 4.2).

As the disc evolves, the protons and neutrons eventually burn to form α particles. At these times the disc is sufficiently cold that the positron and electron capture rates are negligible (i.e, $1/r_{e^-p} \gg t_{\rm visc}$) and Y_e has frozen-out. This fixes the difference between the free neutron and proton mass fractions:

$$X_n - X_p = 1 - 2Y_e. \tag{16}$$

Since the rates for reactions that synthesize and destroy α particles are all fast in comparison to the viscous time, we determine the composition using nuclear statistical equilibrium (NSE) between protons, neutron and α particles. This is expressed by the Saha relation (Shapiro & Teukolsky 1983)

$$X_p^2 X_n^2 = 1.57 \times 10^4 X_\alpha \rho_{10}^{-3} T_{10}^{9/2} \exp\left(-\frac{32.81}{T_{10}}\right). \tag{17}$$

NSE is a good assumption because the disc temperature is generally $\gtrsim 0.5\,{\rm MeV}$ (see Fig. 2), except at very late times or for very low disc masses (e.g. the $M_{\rm d,0} = 0.03\,{\rm M_\odot}$ case, for which we do not calculate the nuclear composition anyways). By combining equations (16) and (17) with mass conservation, $X_p + X_n + X_\alpha = 1$, we solve for all of the mass fractions at a given ρ, T and Y_e.

4 TIME-EVOLVING SOLUTIONS

We next present the results of integrating equations (6), (7) and (15) forward in time. For simplicity, we typically assume that $\dot{J} = 0$. A convenient property of our formalism is the ease with which these complications can be included (for example, we consider the effects of winds at the end of Section 4.1). The disc properties are determined by the initial conditions $M_{\rm d,0}$, $J_{\rm d}$ and $Y_{e,0}$, and by the viscosity α. For the majority of our study we set the initial $Y_{e,0} = 0.1$, which is characteristic of the inner neutron star crust (Haensel
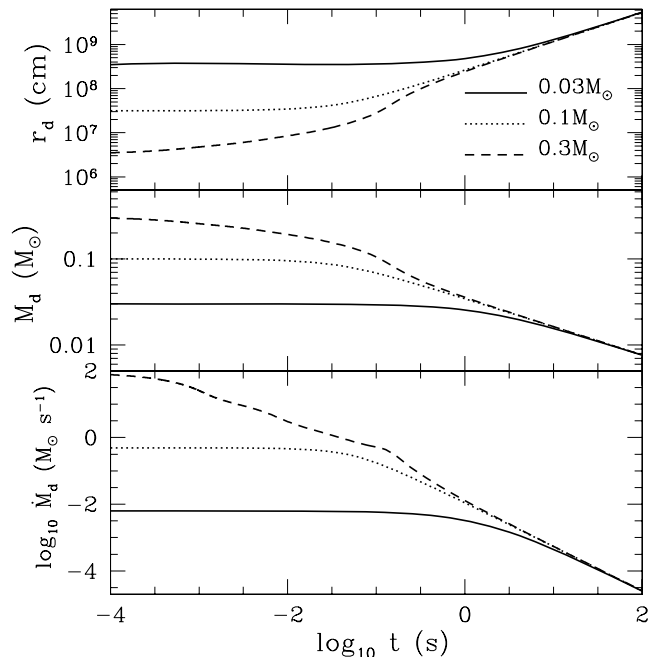

Figure 1. Example disc models showing the evolution of the disc radius, $r_{\rm d}$, disc mass, $M_{\rm d}$, and accretion rate, $\dot{M}_{\rm d}$, as a function of time. We compare $M_{\rm d,0} = 0.03$ (solid lines), 0.1 (dotted lines) and $0.3\,{\rm M_\odot}$ (dashed lines) solutions; all use $J_{49} = 2$ and $\alpha = 0.1$. The inner radius is $r_* \simeq 2.3 r_{\rm g} \simeq 1.02 \times 10^6$ cm (corresponding to a $3\,{\rm M_\odot}$ BH with a spin of $a \simeq 0.9$).

& Zdunik 1990a,b; Pethick & Ravenhall 1995). An additional important parameter is r_*, which is set by the spin of the central BH. In most of our calculations we take $r_* \simeq 2.3 r_{\rm g} \simeq 1.02 \times 10^6$ cm, corresponding to the innermost stable circular orbit of a $3\,{\rm M_\odot}$ BH with spin $a \simeq 0.9$; when calculating the properties of disc outflows in Section 5, however, we also consider the case of a non-rotating ($a = 0$) BH. We consider the general evolution of the disc in Section 4.1, and then focus on the composition in Section 4.2.

4.1 Disc evolution and energetics

At any given time, a ring model is in one of three phases: (1) early time, optically thick to neutrinos and advectively dominated, (2) mid-time, optically thin to neutrinos and geometrically thin, and (3) late time, radiatively inefficient accretion flow (RIAF).[3] This is analogous to the different regions of steady-state, hyperaccreting accretion discs (see e.g. Chen & Beloborodov 2007), but now the transitions occur with time instead of radius. The phases that a certain ring model samples during the course of its viscous expansion depends on $t_{\rm visc,0}$. A more compact disc (a shorter $t_{\rm visc,0}$) will exhibit all three phases, while larger discs may only exhibit phases (2) and (3), or even just (3).

We present a number of figures that are helpful in understanding these three phases and how they are affected by changing $M_{\rm d,0}$. Fig. 1 shows the radius $r_{\rm d}$, mass $M_{\rm d}$ and accretion rate $\dot{M}_{\rm d}$ as a function of time, for $M_{\rm d,0} = 0.3$, 0.1 and $0.03\,{\rm M_\odot}$. Fig. 2 compares the midplane temperature and scaleheight for these same models. Figs 3 and 4 show key results describing the energetics of the $M_{\rm d,0} = 0.3$

---

[3] An optically thick, geometrically thin stage occurs between stages (1) and (2); however, this phase is brief and is not dynamically very different from phase (2), so we do not consider it separately in our discussion.
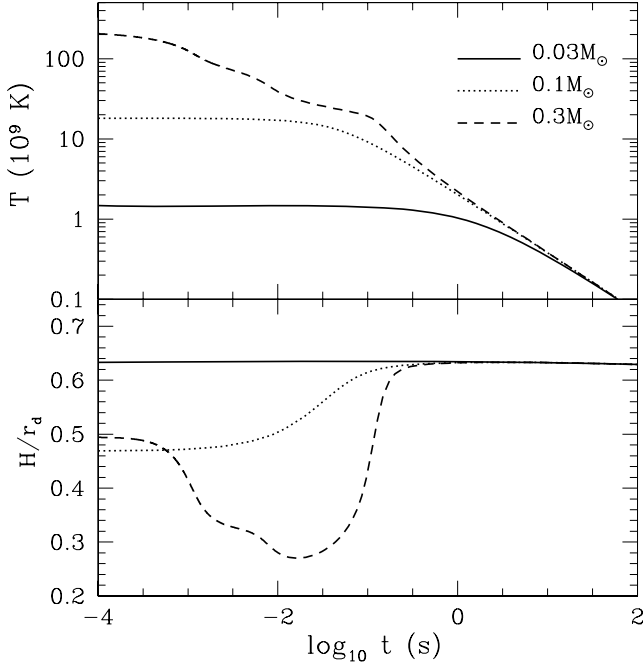
Figure 2. Comparison of the mid-plane temperatures and scaleheight for the three models from Fig. 1. In the lowest mass model, the ring is always advectively dominated, thus H/r_d is constant.
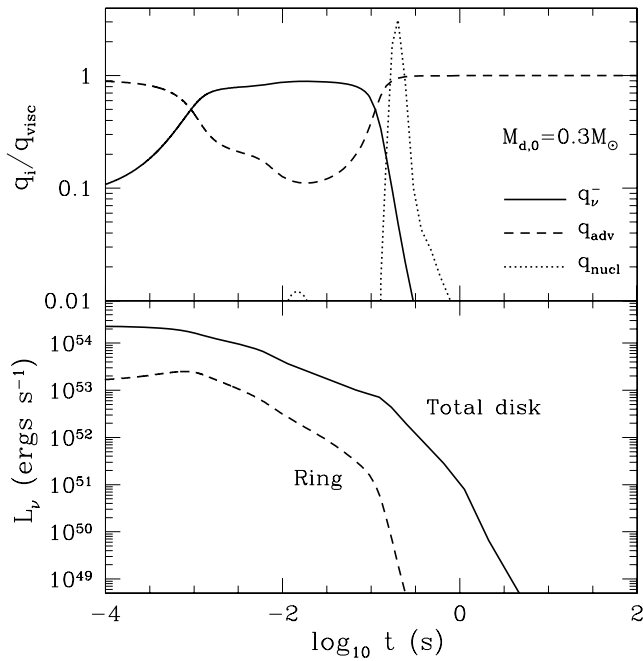

Figure 3. The cooling rates and neutrino luminosity for the $M_{d,0} = 0.3\,M_\odot$ model from Fig. 1. For the cooling rates we compare the neutrino (solid line) and advective (dashed line) rates, normalized to the viscous heating. The implied heating from the creation of α particles is plotted as a dotted line, but is not accounted for in the disc evolution. The neutrino luminosities are from the entire disc (solid line) and the ring (dashed line). The former luminosity is estimated by integrating over a steady-state disc model at each time given $\dot{M}_d(t)$.
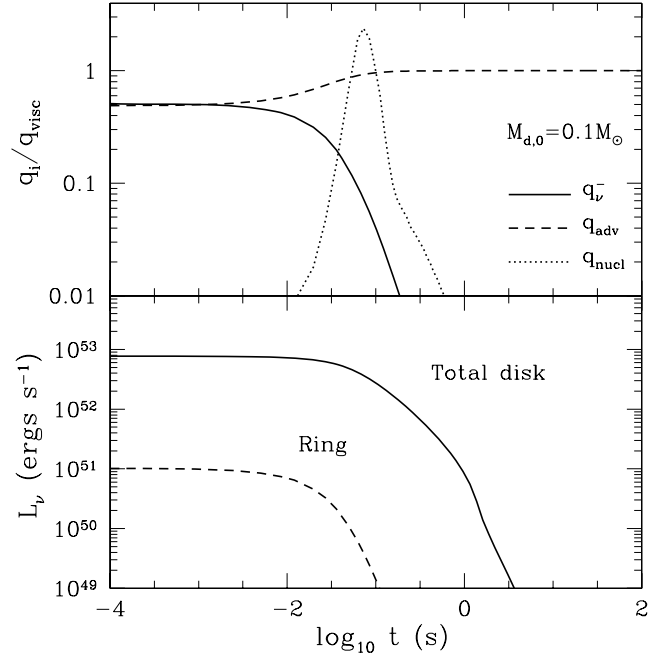
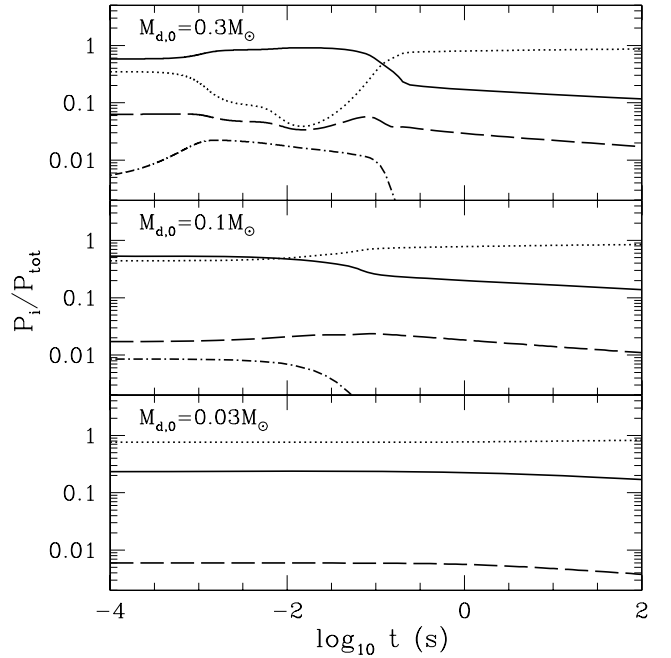**Figure 4.** The same as Fig. 3, but for $M_{d,0} = 0.1\,M_\odot$.

Figure 5. Pressure contributions for $M_{d,0} = 0.3\,M_\odot$ (top panel), $0.1\,M_\odot$ (middle panel) and $0.03\,M_\odot$ (bottom panel). The pressures are all normalized to the total pressure and include the ion pressure (solid lines), radiation pressure (dotted lines), degenerate electron pressure (dashed line) and neutrino pressure (dot–dashed line).

and $0.1\,M_\odot$ solutions, respectively, while Fig. 5 shows the different contributions to the total pressure in the disc as a function of time. Note that we fix the total angular momentum in these calculations ($J_{49} = 2$) and thus a larger $M_{d,0}$ corresponds to a smaller $r_{d,0}$ and a shorter $t_{visc,0}$.

The first transition the discs make is from an optically thick, advective disc to a thin, neutrino-cooled disc; i.e. from phase (1)

to (2). This is only exhibited by the $M_{d,0} = 0.3\,\mathrm{M}_\odot$ model and is seen most clearly at early times in Fig. 2 when $H/r_d \simeq 0.5$ and in Fig. 3 when $q_{adv} \gg q_\nu^-$. Fig. 5 shows that this phase is ion pressure (ideal gas) dominated. A simple estimate determines what initial disc mass is required for phase (1) to occur, i.e. for the initial disc to be optically thick and advective. The disc is advective for radii inside of which the neutrino diffusion time out of the disc exceeds the inflow time. Setting this radius equal to the initial radius of the disc (equation 4), we find that there is a critical disc mass below which the disc never experiences phase (1),

$$M_{d,crit} \sim 0.2\alpha_{0.1}^{-1/10} M_3^{-7/10} \left(\frac{J_{49}}{2}\right)^{9/10} \left(\frac{H}{0.5r_d}\right)^{-3/5} \mathrm{M}_\odot, \qquad (18)$$

where we have dropped scalings with f and A since they appear raised to the 1/10 power. This estimate is consistent with the fact that our $M_{d,1} = 0.1\,\mathrm{M}_\odot$ model is not advective at early times, as seen in Figs 2 and 4. In this case only phases (2) and (3) are seen, i.e. the disc is initially thin and neutrino cooled and later transitions to being advective.

Once the models reach the late-time, RIAF phase, or phase (3), they asymptote to self-similar solutions, independent of the initial disc mass. In this phase, the disc has $q_{adv} > q_\nu^-$ and is radiation pressure dominated. We derive analytic self-similar solutions in Appendix B2 for this limit and show that $r_d \propto t^{2/3}$, $M_d \propto t^{-1/3}$ and $\dot{M}_d \propto t^{-4/3}$. The RIAF solution occurs external to an 'ignition radius', which we estimate as the location where the pair capture cooling rate balances $\sim 1/2$ of the viscous heating for a thick disc,

$$r_{ign} \simeq$$

$$3 \times 10^7 \alpha_{0.1}^{-2} M_3^{-3/5} \left(\frac{H/r_d}{0.4}\right)^{-14/5} \left(\frac{\dot{M}_d}{0.1\,\mathrm{M}_\odot\,\mathrm{s}^{-1}}\right)^{6/5} \mathrm{cm}, \quad (19)$$

where we have scaled H/r_d to ≈ 0.4, a value appropriate for the transition between the thin and thick disc regimes. We combine this with the analytic results for $r_d(t)$ and $\dot{M}_d(t)$ in the RIAF limit (equations B7 and B6)[4] to estimate the time when the disc transitions to being thick, which yields

$$t_{thick} \sim 0.1\alpha_{0.1}^{-23/17} M_3^{-13/17} \left(\frac{J_{49}}{2}\right)^{9/17} \mathrm{s}. \qquad (20)$$

Equation (20) is only applicable if the disc is thin at early times. For sufficiently small initial disc masses, less than

$$M_{d,thick} \sim 0.1\alpha_{0.1}^{2/17} M_3^{-7/17} \left(\frac{J_{49}}{2}\right)^{14/17} \mathrm{M}_\odot, \qquad (21)$$

this is no longer true, and the disc is always a RIAF at its outer radius.

Figs 3 and 4 show that at approximately the same time as the disc transitions from being thin to thick, protons and neutrons are fused to He. Although the nuclear heating rate q_{nuc} is shown in Figs 3 and 4, this heating was not included in our time-dependent calculations so that we could obtain solutions at late times. The nuclear heating rate is sufficiently large, i.e. $q_{nucl} \gtrsim q_{visc}$, that the disc is not able to accommodate this added energy (it is already thick with $H \simeq r$ due to viscous heating alone). This probably implies that the burning contributes to driving a powerful wind (as described by Lee & Ramirez-Ruiz 2007).

However, such a wind already begins at this time by virtue of the disc being advective (as discussed in Section 5.2). In Appendix B3,
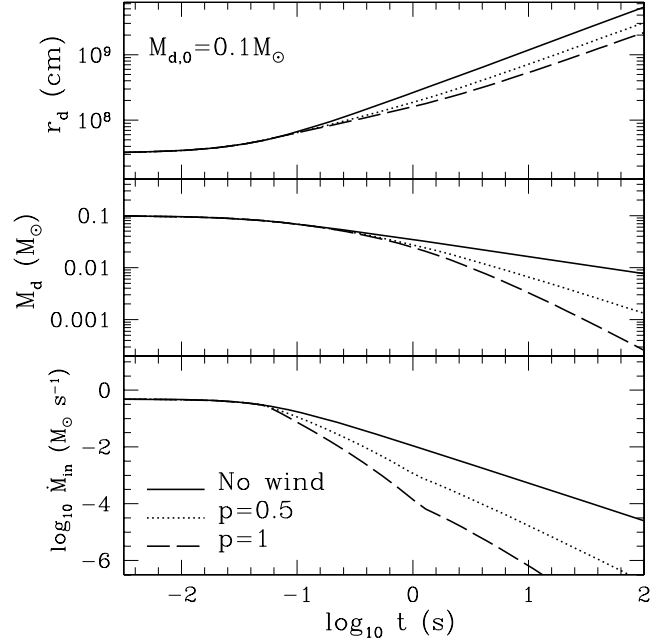

Figure 6. The radius r_d, disc mass M_d and mass accretion rate reaching the central BH, $\dot{M}_{in}$, for different parametrizations of mass loss during the advective phase. We initialize a disc with $M_{d,0} = 0.1\,\mathrm{M}_\odot$ (and all other parameters fixed as in Fig. 1) and compare solutions with no wind (solid line), $p = 0.5$ (dotted line; see equation B8) and $p = 1$ (dashed line).

we present analytic self-similar solutions for advective discs with mass loss and show that this significant mass loss causes M_d and $\dot{M}_d$ to decline much more rapidly with time than is shown in Fig. 1. This is shown explicitly in Fig. 6, where we present disc models calculated using the mass and angular momentum loss prescriptions described in Appendix B3; such losses are assumed to occur only when the disc is thick, between $\sim \max(r_*, r_{ign})$ and $\sim r_d$. Fig. 6 compares time-dependent solutions with no wind (solid line), a wind with $p = 0.5$ (dotted line; see equation B8), and a wind with $p = 1$ (dashed line).[5] The loss of angular momentum does not appreciably slow the radial expansion of the disc, but it does substantially accelerate the decline in the disc mass and accretion rate (see also equations B12 and B13). If the models with winds are accurate, significant accretion is only likely to last for a few viscous times once the disc enters the late-time advective phase. Continued central engine activity at much later times could result from late-time infall of tidally stripped NS material (e.g. Lee & Ramirez-Ruiz 2007).

As an additional comparison, we present the effect of varying J_d in Fig. 7. The main trend is that a higher J_d has a larger initial radius for a given M_d, and therefore a longer viscous time and smaller accretion rate. The late time behavior is more sensitive to J_d than the initial M_d, as predicted by the self-similar solutions, but it still does not affect the late-time disc radius (see equation B7). We do not plot our results for different α since they are generally consistent with the analytic scalings above and in Appendix B.

4.2 Composition

The composition of the disc is important for determining the observational effects of any outflows. To this end, we plot the composition

---

[4] We use these solutions rather than the thin-disc ones because the numerical results follow these more closely (Fig. B1).

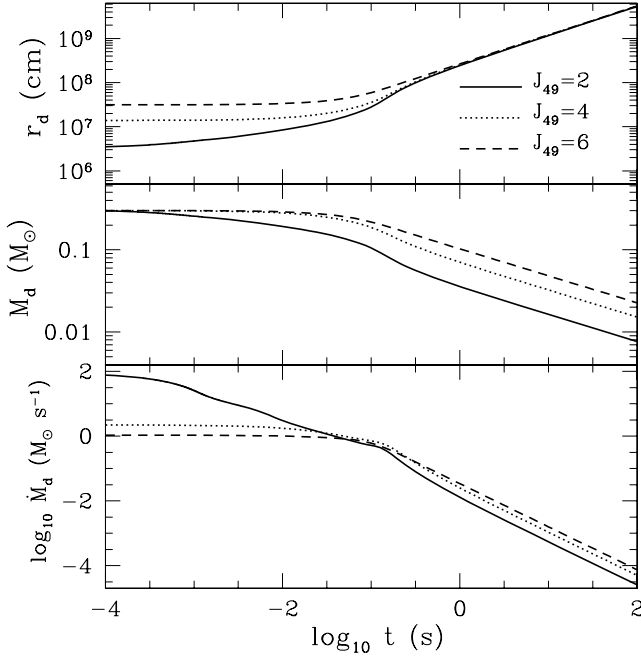[5] See Appendix B2 for the definition of p.

Figure 7. Similar to Fig. 1, but now taking the angular momentum to be $J_{49} = 2$ (solid lines), 4 (dotted lines) and 6 (dashed lines). All solutions take $M_{d,0} = 0.3\,M_\odot$ with all other variables the same as in Fig. 1.

of our $M_{d,0} = 0.3\,M_\odot$, $J_{49} = 2$ disc as a function of time in the upper panel of Fig. 8. In the bottom panel we plot the relevant time-scales for setting the composition, namely the viscous time-scale, t_{visc} (solid line), the neutronization time-scale $t_n = 1/r_{e-p}$ (dotted line),
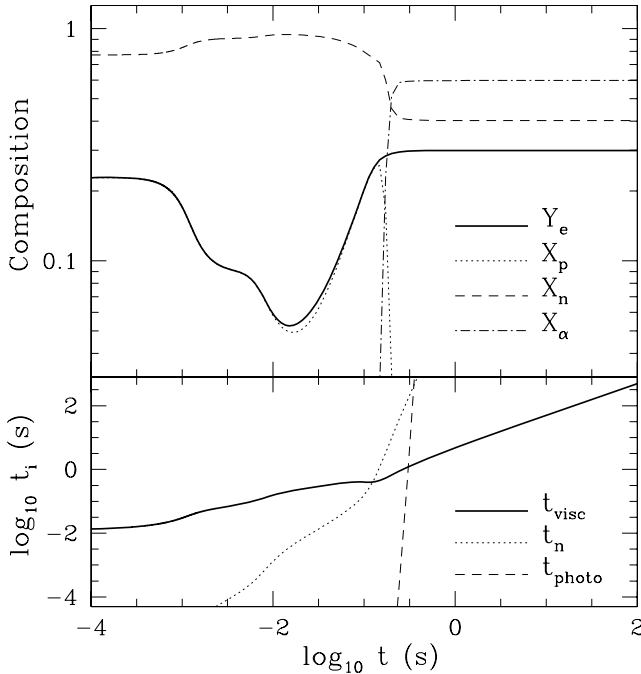

Figure 8. The composition and important reaction time-scales as a function of time, for the $M_{d,0} = 0.3\,M_\odot$ model from Fig. 1. In the top panel we plot the electron fraction, Y_e, and the mass fraction of protons, neutrons and α particles (see inset key). In the bottom panel we show the viscous time, t_{visc} (thick, solid line), the neutronization time, $t_n = 1/r_{e-p}$ (dotted line), and the α particle photodisintegration time, t_{photo} (dashed line).
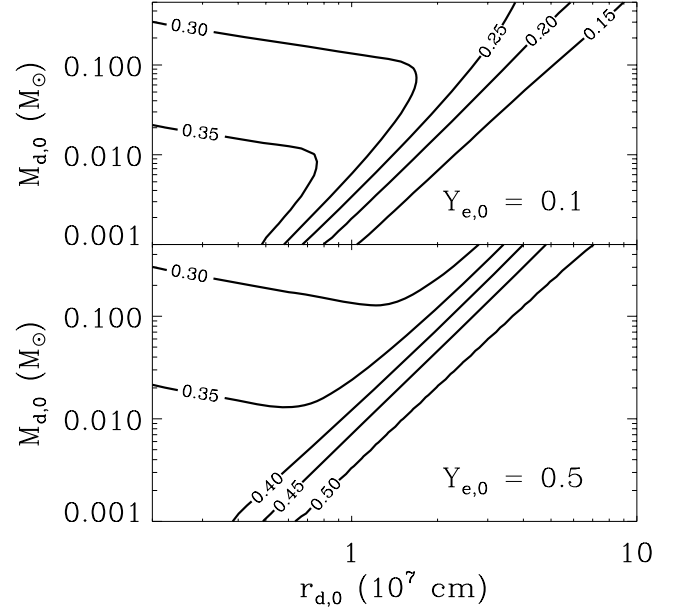

Figure 9. Contours of late-time electron fraction in the expanding disc as a function of initial disc mass $M_{d,0}$ and radius $r_{d,0}$, for two different initial compositions. Relatively compact discs come into β equilibrium and reach an electron fraction independent of the initial Y_e, while low mass, more extended discs retain their initial composition. Fig. 8 shows the evolution of Y_e with time for one particular disc solution.

and the time-scale for α particle photodisintegration, t_{photo} (dashed line). At early times $t_n \ll t_{visc}$, so that an equilibrium value of $Y_e \simeq 0.23$ is reached almost immediately. As the disc leaves the optically thick phase and becomes thinner, degeneracy pressure plays a larger role. This enhances neutron production, with a minimum $Y_e \simeq 0.05$. As the neutrino cooling subsides and the disc becomes thick again, Y_e increases. Before Y_e can reach $\simeq 0.5$, it freezes-out at a value of $Y_e \simeq 0.3$ once $t_n > t_{visc}$.

Besides the neutron abundance, Fig. 8 also highlights the production of α particles. Initially, the reactions needed to convert neutrons and protons to helium as well as photodisintegration of helium all happen on time-scales much shorter than the disc evolution time-scale (as an example, we plot the helium photodisintegration time-scale in the bottom panel of Fig. 8), so that we can estimate the α particle mass fraction using chemical balance (equation 17). Once the α particle photodisintegration time-scale becomes sufficiently long ($t_{visc} < t_{photo}$), chemical equilibrium no longer applies and $X_p = 0$, $X_n = 1 - 2Y_e \simeq 0.4$ and $X_\alpha = 2Y_e \simeq 0.6$.

Fig. 9 shows how the late-time, frozen-out value of Y_e in the disc depends on the initial disc mass $M_{d,0}$ and radius $r_{d,0}$, for two different initial electron fractions, $Y_{e,0} = 0.1$ and 0.5. The former is relevant for the discs created from NS–NS or BH–NS mergers (the focus of this paper), while a larger $Y_{e,0} \simeq 0.5$ is appropriate for discs created during the accretion-induced collapse (AIC) of a white dwarf to a neutron star (e.g. Woosley & Baron 1992; Dessart et al. 2006). Fig. 9 shows that for sufficiently compact discs, the disc reaches a modestly neutron-rich composition, with $Y_e \simeq 0.3$–0.4, independent of the initial composition. This is because, as highlighted in Fig. 8, the time-scale to come into β equilibrium is shorter than the viscous time. For discs with a small initial mass and/or a large initial radius (the lower right-hand corner of each panel), $t_n > t_{visc}$ and the disc retains its initial composition (set by the tidally disrupted progenitor and the subsequent dynamical

stage of the merger). Finally, neutrino irradiation of the outer disc by the inner disc can increases the freeze-out electron fraction, but we estimate this changes the freeze-out value of Y_e by at most ~ 20 per cent.[6]

5 DISC WINDS

Having described the evolution of the accretion disc as a function of time, we now discuss the properties of outflows from these hyperaccreting discs. Winds driven from deep within the BH potential well could produce relativistic jets and power late-time central engine activity. Outflows driven from larger radii dominate the system's mass loss and may power supernova-like optical transients through the decay of radioactive isotopes that are synthesized in the wind (Li & Paczyński 1998; Kulkarni 2005). In both cases, the mass-loss rate and nuclear composition are critical for determining the observable signature.

The type and character of the outflow depends on the disc's thermodynamic state and changes as it passes through the different stages of evolution described in the previous section. In Section 5.1 we discuss early times when winds are due to neutrino irradiation of the thin, efficiently neutrino-cooled portions of the disc. We then consider thermally driven winds during thick, radiatively inefficient accretion in Section 5.2. This dominates the mass loss at late times and blows away most of the remaining disc. In Section 5.3 we summarize the nuclear composition of the outflows during each phase. We predict an ejected ^{56}Ni mass of at most $\sim 10^{-3}\,M_\odot$ (Section 5.4). Its decay may power transient emission detectable following some short GRBs.

5.1 Neutrino-heated thin-disc winds

A wind with a mass loss rate $\dot{M}_w$ driven from a thin disc at radius r must absorb a net power greater than $\dot{E}_b = GM\dot{M}_w/2r$ to become unbound from the central BH. In principle, $\dot{E}_b$ may be supplied by dissipation of the turbulence that produces the accretion shear stresses. 'Viscous' heating of this kind only efficiently drives an outflow if a substantial fraction of the accretion power is dissipated in the disc's upper atmosphere, where the cooling time-scale is long compared to the wind's outward advection time-scale. However, local radiation magnetohydrodynamic (MHD) simulations to date suggest that very little energy dissipation occurs in the corona (e.g. Krolik, Hirose & Blaes 2007). Instead, heating in the atmosphere above a thin, neutrino-cooled disc is likely dominated by neutrino irradiation. We therefore focus on the neutrino-driven mass-loss rate, which sets a *minimum* $\dot{M}_w$, and which can be reliably estimated. Neutrino-driven outflows from hyperaccreting discs have also been studied by Daigne & Mochkovitch (2002), Levinson (2006), Barzilay & Levinson (2008) and Metzger, Thompson & Quataert (2008, hereafter M08b); Dessart et al. (2008b) calculate the neutrino-driven mass loss from the central NS following a NS–NS merger under the assumption that collapse to a BH is not prompt.

The neutrino-driven mass-loss rate is calculated by equating $\dot{E}_b$ to the total neutrino heating rate in the disc's atmosphere. For the

radii and entropies that characterize the winds, heating via electron neutrino absorption on baryons ($p + \bar{\nu}_e \rightarrow n + e^+$ and $n + \nu_e \rightarrow p + e^-$) dominates other forms of neutrino heating (e.g. $\nu - \nu$ annihilation and $\nu - e^-$ scattering; see Qian & Woosley 1996, hereafter QW96). Since the neutrino absorption cross-section, $\sigma_{\nu N} \simeq 5 \times 10^{-44}\,\langle \epsilon_\nu^2 \rangle\,\mathrm{MeV}^{-2}\,\mathrm{cm}^2$, increases with neutrino energy, neutrinos radiated from near the inner radius r_* dominate. Assuming that the ν_e and $\bar{\nu}_e$ luminosities and spectra are approximately equal and can be approximated as originating from a point source at small radii, the neutrino heating rate through a surface density Σ at radius r is

$$q_\nu^+ = \frac{L_\nu \sigma_{\nu N} \Sigma}{4\pi m_N r^2} \simeq 2 \times 10^{39} L_{52} \langle \epsilon_{10}^2 \rangle \Sigma_{18} r_6^{-2}\,\mathrm{erg\,s^{-1}\,cm^{-2}}, \quad (22)$$

where $r = 10^6\,r_6$ cm, $L_\nu = 10^{52}\,L_{52}$ erg s^{-1}, $\langle \epsilon_\nu^2 \rangle = 100 \langle \epsilon_{10}^2 \rangle$ MeV^2 and $\Sigma = \Sigma_{18}\,10^{18}$ g cm^{-2}. This expression assumes that the absorbing layer is optically thin, i.e. that $\tau_\nu \equiv \Sigma \sigma_{\nu N}/m_N \simeq 3\Sigma_{18} \langle \epsilon_{10}^2 \rangle < 1$.

First, consider neutrino heating in comparison to viscous heating in the mid-plane. This ratio is largest when the disc is marginally optically thick ($\tau_\nu \simeq 1$), peaking at a value of

$$\left.\frac{q_\nu^+}{q_{\mathrm{visc}}}\right|_{\tau_\nu \simeq 1}$$
$$\simeq 0.5 \left(\frac{\epsilon}{0.1}\right)\left(\frac{f}{1.6}\right)\left(\frac{A}{3.6}\right)^{3/5} \langle \epsilon_{10}^2 \rangle^{2/5} J_{49}^{2/5} M_3^{-6/5}, \quad (23)$$

where $\epsilon \equiv L_\nu/\dot{M}_d c^2$ is the disc's radiative efficiency. Thus, although we neglected neutrino heating in Section 4, it may become somewhat important when $\tau_\nu \sim 1$ and should be included in a more detailed calculation.

We now consider a wind that emerges from the disc in the z direction, parallel to the rotation axis. Away from the disc mid-plane, neutrino heating dominates over viscous heating, balancing cooling ($q_\nu^+ = q_\nu^-$) at a slightly lower temperature, $T_\nu \simeq 3.3 L_{52}^{1/6} \langle \epsilon_{10}^2 \rangle^{1/6} r_6^{-1/3}$ MeV. Moving further out in the hydrostatic atmosphere, the temperature slowly decreases below T_ν. Because of the strong temperature dependence of the pair capture cooling rate ($q_\nu^- \propto T^6$), a 'gain region' of net neutrino heating (i.e. $q_\nu^+ > q_\nu^-$) develops above a height z_{gain}. This net heating drives an outflow.

The thermal power deposited in the upper disc atmosphere $\dot{E}_\nu$ is the specific heating rate q_ν^+/Σ (equation 22) multiplied by the mass of the atmosphere in the gain region $M_{\mathrm{gain}} \simeq 2\pi H(z_{\mathrm{gain}})r^2 \rho(z_{\mathrm{gain}})$, where $H(z_{\mathrm{gain}})$ is the scaleheight near the base of the gain region. Although the mid-plane of a neutrino-cooled disc is generally dominated by non-relativistic gas pressure (see Fig. 5), the gain region has a sufficiently low density that it is instead dominated by radiation pressure $P_{\mathrm{rad}} = (11/12)aT^4$. Its scaleheight is $H(z_{\mathrm{gain}}) \simeq (P_{\mathrm{rad}}/\rho g_z)|_{z_{\mathrm{gain}}}$, where g_z is the gravitational acceleration in the z direction. Since $H(z_{\mathrm{gain}})$ is less than the mid-plane scaleheight H, $z_{\mathrm{gain}} \simeq H$ and $g_z \simeq GMH/r^3$. The atmosphere in the gain region is roughly isothermal so we set $T(z_{\mathrm{gain}}) \approx T_\nu$. By combining these estimates and equating $\dot{E}_\nu$ with $\dot{E}_b$ we find that the neutrino-driven mass-loss rate from a thin disc is

$$\dot{M}_\nu|_{S^a \gg S_N} \approx 10^{-6} L_{52}^{5/3} \langle \epsilon_{10}^2 \rangle^{5/3} r_6^{5/3} M_3^{-2} (H/r)^{-1}\,M_\odot\,\mathrm{s^{-1}}, \quad (24)$$

analogous to that derived by QW96 for protoneutron star winds. The assumption that the atmosphere is radiation dominated is only valid if the asymptotic entropy in relativistic particles S^a exceeds that in non-relativistic nucleons $S_N \simeq 6 + \ln(T_{\mathrm{MeV}}^{3/2}/\rho_{10})\,k_B$ baryon^{-1}, where $T = T_{\mathrm{MeV}}$ MeV. By dividing the energy gained by a nucleon in the wind $\simeq GMm_N/2r$ by the gain region temperature $T(z_{\mathrm{gain}})$,

---

[6] Our calculations employ the pair-capture cooling prescription of DiMatteo et al. (2002), which assume $Y_e = 0.5$ and ultrarelativistic electrons; we find, however, that including the effects of degeneracy and arbitrary electron energies on the cooling changes the asymptotic electron fraction by at most a few per cent.

we estimate

$$S^a \simeq 60 L_{52}^{-1/6} \langle \epsilon_{10}^2 \rangle^{-1/6} r_6^{-2/3} M_3 \ k_B \ \mathrm{baryon^{-1}} \qquad (25)$$

as the asymptotic wind entropy.

Although equation (24) does not strictly hold when $S^a \sim S_N$, QW96 show that $\dot{M}_\nu$ scales the same way with L_ν, $\langle \epsilon_\nu^2 \rangle$, M and r, but with a larger normalization of

$$\dot{M}_\nu|_{S^a \sim S_N} \approx 10^{-5} L_{52}^{5/3} \langle \epsilon_{10}^2 \rangle^{5/3} r_6^{5/3} M_3^{-2} (H/r)^{-1} \, \mathrm{M_\odot \, s^{-1}}. \qquad (26)$$

The mass-loss rate is higher for low-entropy winds because neutrino heating peaks further off the disc surface, which reduces the binding energy and gravitational acceleration of matter in the gain region. Using the numerical disc wind calculations described in M08b we have verified that equation (26) holds to within a factor of $\simeq 2$ when $S^a \sim S_N$.

In deriving equations (24) and (26), we have implicitly assumed that the time-scale for neutrinos to heat matter in the gain region $t_{\mathrm{heat}} \equiv (U_{\mathrm{th}} \Sigma / \rho q_\nu^+)|_{z_{\mathrm{gain}}}$, where $U_{\mathrm{th}} \simeq 3P_{\mathrm{rad}}$ is the thermal energy density, is short compared to t_{visc}, the time-scale over which the disc properties appreciably change. Equating S^a (equation 25) to the entropy in relativistic particles $\propto T^3/\rho$, we find that

$$\rho(z_{\mathrm{gain}}) \simeq 10^8 r_6^{-1/3} L_{52}^{2/3} \langle \epsilon_{10}^2 \rangle^{2/3} M_3^{-1} \, \mathrm{g \, cm^{-3}}. \qquad (27)$$

Then, using equations (22) and (27), we have that[7]

$$t_{\mathrm{heat}} \simeq \left. \frac{3 P_{\mathrm{rad}}}{\rho(q_\nu^+/\Sigma)} \right|_{z_{\mathrm{gain}}} \simeq 0.1 \, \mathrm{s} \, L_{52}^{-1} r_6 \langle \epsilon_{10}^2 \rangle^{-1} M_3. \qquad (28)$$

For most of the disc solutions considered in this paper, we find that $t_{\mathrm{heat}} \lesssim t_{\mathrm{visc}}$ during the thin-disc phase; thus, equations (24) and (26) are reasonably applicable near r_d.

Fig. 10 compares the accretion rate $\dot{M}_d$ (solid line) with the neutrino-driven mass-loss rate $\dot{M}_\nu$. In order to determine L_ν and $\langle \epsilon_\nu^2 \rangle$, we calculated steady-state disc models (e.g. DiMatteo et al. 2002) with the accretion rate set at each time according to our ring model with $J_{49} = 2$ and $M_d = 0.3 \, \mathrm{M_\odot}$. We plot the neutrino-driven mass-loss rate $\dot{M}_\nu$ (equations 24 and 26) at small (dotted line) and large (short-dashed line) radii. This shows that the mass loss is dominated by large radii where the majority of the mass lies, as expected since $\dot{M}_\nu \propto r^{5/3}$. The vertical dot–dashed line marks where the disc transitions to being thick (equation 20), after which neutrino heating no longer dominates the wind mass loss.

Outflows that are launched from small radii, near r_*, have the greatest potential to produce relativistic jets and to power high energy emission. However, as we now argue, these neutrino-driven winds are too massive to become highly relativistic. Our calculation above focused on purely thermal, neutrino-driven winds, which accelerate matter to only a fraction of the escape speed (and thus are mildly relativistic). However, in the presence of a strong, large-scale open poloidal magnetic field, a more powerful, magnetically driven outflow is possible. Magnetocentrifugal support in the wind's hydrostatic atmosphere may further enhance mass loss (e.g. Levinson 2006), but equation (24) still represents the *minimum* mass loading on field lines which thread a neutrino-cooled disc. Fig. 10 shows that $\dot{M}_\nu(r_*) \sim 10^{-4}$–$10^{-2} \, \mathrm{M_\odot \, s^{-1}}$ during the thin disc phase. The luminosities of the prompt emission and late-time X-ray flares from short GRBs, however, do not typically exceed $L_\gamma \sim 10^{50} \, \mathrm{erg \, s^{-1}}$ (and are often much lower; Nakar 2007). Thus, even assuming a modest radiative efficiency for the outflow of $\epsilon_w \sim 0.1$, the Lorentz factor Γ
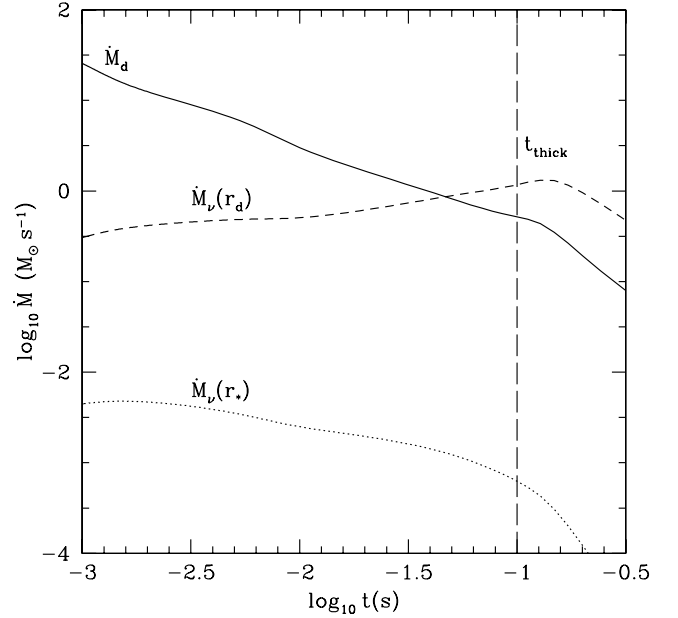

Figure 10. The accretion rate $\dot{M}_d$ (solid line) and neutrino-driven mass-loss rates $\dot{M}_\nu$ for our $J_{49} = 2$ and $M_{d,0} = 0.3 \, \mathrm{M_\odot}$ model, focusing on the phase of thin, efficiently neutrino-cooled accretion. The neutrino-driven mass-loss rate $\dot{M}_\nu$ (interpolated between equations 24 and 26) is shown at the inner disc radius ($r_* = 10^6$ cm; dotted line) and at the outer disc radius (near r_d; short-dashed line). The disc is advective to the right of the vertical line (equation 20), at which point the mass loss will no longer be dominated by neutrino irradiation.

of a neutrino-heated disc wind must obey $\Gamma \simeq L_\gamma / [\epsilon_w \dot{M}_\nu(r_*) c^2] \lesssim 5$, which is inconsistent with existing compactness constraints on short GRBs (Nakar 2007). A more likely source for the relativistic outflows that power short GRBs and their late-time flares are nearly baryon-free field lines which thread the BH's event horizon (e.g. McKinney 2005). In addition, in Section 5.2 we argue that when the disc becomes advection dominated and neutrino irradiation effectively ceases, jet production may be more likely.

5.2 Radiatively inefficient thick-disc winds

At late times ($t \sim t_{\mathrm{thick}}$; equation 20) the disc transitions from thin and neutrino cooled to being advective. At this point a neutrino-driven outflow is unlikely to dominate the mass loss, in part because the neutrino luminosity precipitously drops (Figs 3 and 4). In addition, because RIAFs possess a positive Bernoulli parameter, a powerful viscously driven outflow is likely (Blandford & Begelman 1999; Stone & Pringle 2001; Proga & Begelman 2003).

In Section 4.1 we showed that the disc becomes radiatively inefficient external to an 'ignition radius' $r_{\mathrm{ign}} \propto \dot{M}_d^{6/5}$ (equation 19). The outer disc, near r_d, thickens first (when $r_d \sim r_{\mathrm{ign}}$ at $t \sim t_{\mathrm{thick}}$) and radiatively inefficient conditions move inwards as $\dot{M}_d$ decreases. In the simplest picture, one might expect that the innermost radii become an RIAF only once $\dot{M}_d$ drops from its value at $t \sim t_{\mathrm{thick}}$ by an additional factor $\sim (r_*/r_d)^{5/6}$. In fact, the *entire* disc probably become radiatively inefficient on a time-scale similar to t_{thick} if the accretion rate which reaches small radii abruptly decreases once the outer disc thickens (Fig. 6). Hence, at a time t_{thick}, a significant portion of the accreting matter may be redirected into an outflow, with only a fraction $\sim (r_*/r_d)$ reaching small radii and accreting on to the BH (Stone & Pringle 2001).

---

[7] Equation (28) is also approximately equal to the outward advection time-scale of the wind in the heating region.

X-ray binaries typically produce radio jets upon transitioning from their 'high-soft' (radiatively efficient) to 'low-hard' (radiatively inefficient) states (e.g. Remillard & McClintock 2006). In analogy, once the inner disc becomes an RIAF, conditions seem to favour the production of relativistic jets (see also Lazzati, Perna & Begelman 2008).[8]

Even if only a fraction (r_*/r_d) of the mass remaining when the disc thickens actually reaches the origin, the total energy supply available would be

$$E_{jet} \equiv \epsilon_{jet} M_d(t_{thick}) c^2 \left[\frac{r_*}{r_d(t_{thick})} \right]$$

$$\simeq 3 \times 10^{50} \left(\frac{\epsilon_{jet}}{0.1} \right) \left(\frac{r_*}{10^6 \, cm} \right) \alpha_{0.1}^{6/17} M_3^{-4/17} \left(\frac{J_{49}}{2} \right)^{8/17} \, erg,$$

$$\tag{29}$$

where ϵ_{jet} is the fraction of the accretion energy used to power a jet and we have estimated $M_d(t_{thick})$ and $r_d(t_{thick})$ using the self-similar thick-disc solutions (equations B5 and B7, respectively). Equation (29) shows that the accretion energy available from near r_* following the RIAF transition is more than sufficient to power the late-time X-ray flares observed following some short GRBs. If this is the case, t_{thick} sets a characteristic time-scale for late-time central engine activity. If $\alpha \lesssim 10^{-3}$, t_{thick} may be large enough to explain the ~30 s delay until flaring observed for some short GRBs (e.g. Berger et al. 2005; Villasenor et al. 2005). However, very late time energy injection, such as the *Chandra* flare observed two weeks after GRB 050709 (Fox et al. 2005), appears to require an alternative explanation. In addition, given observational evidence for $\alpha \sim 0.1$ in a number of environments (King, Pringle & Livio 2007), it may be more natural to associate E_{jet} and t_{thick} with the energy and duration, respectively, of the short GRB itself, rather than the late-time central engine activity (see Section 6).

5.3 Outflow nuclear composition

The outflow nuclear composition has important consequences for the observable signature of compact object mergers. Non-relativistic outflows are sufficiently dense to synthesize heavy isotopes (Pruet, Thompson & Hoffman 2004; Surman, McLaughlin & Hix 2006), which may power transient emission via radioactive decay. The isotopic yield depends on the speed, thermodynamic properties and the asymptotic electron fraction Y_e^a in the outflow.[9] Although relativistic winds from the inner disc are unlikely to synthesize anything heavier than He (Lemoine 2002; Beloborodov 2003b), Y_e^a is important in this case as well. A neutron-rich outflow may alter the jet's dynamics and the prompt and afterglow emission from that of the standard GRB fireball model (e.g. Derishev, Kocharovsky & Kocharovsky 1999; Beloborodov 2003a; Rossi, Beloborodov & Rees 2006).

Fig. 11 delineates different regimes of outflow properties and composition (as given by Y_e^a) as a function of the wind launching radius r and accretion rate $\dot{M}_d$. We fix $\alpha = 0.1$ and $M = 3 \, M_\odot$. The time-dependent evolution of the ring radius r_d is shown for a solution with $J_{49} = 2$ and $M_{d,0} = 0.3 \, M_\odot$ (solid line). At each time a given steady-state disc profile can be read off of this plot
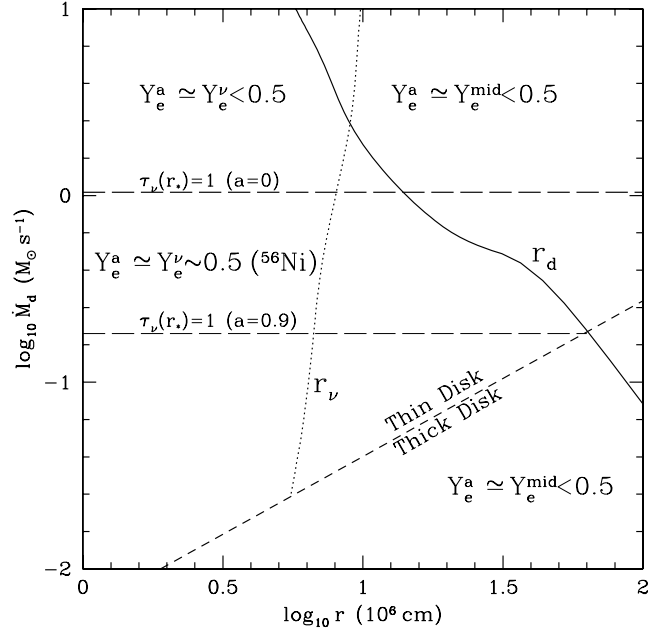
Figure 11. Asymptotic electron fraction Y_e^a for disc winds as a function of the wind launching radius r and accretion rate $\dot{M}_d$ (for $\alpha = 0.1$ and $M = 3 \, M_\odot$). The solid line indicates the location of the ring radius r_d for our fiducial solution with $M_{d,0} = 0.3 \, M_\odot$ and $J_{49} = 2$. The short dashed line is the 'ignition' radius r_{ign} (equation 19). Exterior to this (marked 'Thick Disc') the disc is advective with a viscously driven wind of composition $Y_e^a \simeq Y_e^{mid} < 0.5$. Interior to r_{ign} (marked 'Thin Disc') a neutrino-driven wind occurs. The dotted line shows $r = r_\nu$ with $Q = 2$ (equation 30) and determines where the neutrino absorptions necessary to unbind matter alter the wind composition, so that $Y_e^a \simeq Y_e^{mid} < 0.5$ ($Y_e^a \simeq Y_e^\nu$) exterior (interior) to r_ν. The $\dot{M}_d$ above which $\tau(r_*) > 1$ is plotted for BH spins of $a = 0$ and 0.9. Above this line, the $\bar{\nu}_e$ and ν_e spectra differ and $Y_e^\nu < 0.5$, while below this their spectra are similar and $Y_e^\nu \simeq 0.5$. In the region where $r < r_{ign}$, $\tau_\nu(r_*) < 1$ and $r < r_\nu$ (i.e. the middle/lower left-hand trapezoid), $Y_e^a \simeq Y_e^\nu \sim 0.5$; these conditions are favorable for ^{56}Ni production (see Section 5.4).

as a horizontal line that extends from the far left and ends on r_d. Therefore, outflows from radii *interior* to r_d contribute to the disc's total nucleosynthetic yield.

The ignition radius r_{ign} (equation 19) is shown in Fig. 11 with a short dashed line. For $r \gtrsim r_{ign}$ the disc is an RIAF and marked in the figure as 'Thick Disc'. In this case, a viscously driven outflow dominates (Section 5.2). Since outflows from RIAFs escape the disc in roughly the accretion time-scale, these winds retain the mid-plane electron fraction (M08b), so that $Y_e^a \simeq Y_e^{mid} \ll 0.5$ (because the disc itself freezes-out neutron rich, as summarized in Section 4.2 and Fig. 9).

For $r \lesssim r_{ign}$, the disc is efficiently neutrino cooled and marked in Fig. 11 as 'Thin Disc'. The absorption of neutrinos, which heats the outflow and unbinds it from the BH may also alter its nucleonic composition. This drives Y_e^a to a value set by the neutrino radiation field Y_e^ν, which in general is different from Y_e^{mid}. A simple criterion was discussed by M08b for determining when $Y_e^a \simeq Y_e^\nu$. A typical nucleon in the accretion disc at radius r must absorb an energy $\simeq G M m_N / 2r$ to become unbound from the BH, so that $N_\nu \simeq G M m_N / 2r \langle \epsilon_\nu \rangle$ neutrinos must be absorbed per nucleon. If we take $N_\nu > Q \sim 2$–3, then a typical nucleon has changed its identity ($p \rightarrow n$ or $n \rightarrow p$) at least several times.

---

[8] This is in stark contrast to jets powered by neutrino annihilation along the polar axis, which require a *high* radiative efficiency.

[9] The *asymptotic* electron fraction is germane because heavy nuclei primarily form after freeze-out from β equilibrium.

This implies that all purely neutrino-driven outflows from radii smaller than

$$r_\nu \equiv \frac{GMm_p}{2Q\langle\epsilon_\nu\rangle} \simeq 10^7 M_3 \langle\epsilon_{10}\rangle^{-1}(Q/2)^{-1} \text{ cm}, \tag{30}$$

where $\langle\epsilon_\nu\rangle \equiv 10\langle\epsilon_{10}\rangle$ MeV, achieve $Y_e^a \simeq Y_e^\nu$, independent of the disc's mid-plane composition.

We plot r_ν with $Q = 2$ as a dotted line in Fig. 11, where $\langle\epsilon_\nu\rangle$ is calculated from $\dot{M}_d$ using our steady-state disc solutions (see Section 5.1). For $r \lesssim r_\nu$, any neutrino-driven outflow enters equilibrium with the neutrino radiation field (i.e. $Y_e^a \simeq Y_e^\nu$). For $r \gtrsim r_\nu$ the outflow approximately retains the mid-plane electron fraction (i.e. $Y_e^a \simeq Y_e^{mid}$).

Although we have established the conditions under which Y_e^a is determined by neutrino absorptions, we must now address what sets Y_e^ν itself. If the rate of neutrino absorptions exceeds the rate of degenerate pair captures before the wind falls out of β equilibrium, Y_e^ν is

$$Y_e^\nu \equiv \left(1 + \frac{L_{\bar{\nu}_e}}{L_{\nu_e}} \frac{\langle\epsilon_{\bar{\nu}_e}\rangle - 2\Delta + 1.2\Delta^2/\langle\epsilon_{\bar{\nu}_e}\rangle}{\langle\epsilon_{\nu_e}\rangle + 2\Delta + 1.2\Delta^2/\langle\epsilon_{\nu_e}\rangle}\right)^{-1}, \tag{31}$$

where $\Delta = 1.293$ MeV is the neutron–proton mass difference, and $L_{\nu_e}/L_{\bar{\nu}_e}$ and $\langle\epsilon_{\nu_e}\rangle/\langle\epsilon_{\bar{\nu}_e}\rangle$ are the mean $\nu_e/\bar{\nu}_e$ luminosities and energies, respectively, from a centrally concentrated source (Qian et al. 1993; QW96). Equation (31) demonstrates that the ν_e and $\bar{\nu}_e$ spectra are crucial for setting Y_e^ν.

Since the disc's luminosity and temperature peak at just a few r_g, Y_e^ν is primarily determined by conditions at small radii. At early times, the accretion disc may be optically thick near r_* and so the ν_e and $\bar{\nu}_e$ spectra depend on the temperatures at ν_e and $\bar{\nu}_e$ neutrinospheres, respectively. Since there are more neutrons than protons in the disc, the optical depth to ν_e through the disc is higher than to $\bar{\nu}_e$; thus, the temperature at the $\bar{\nu}_e$ neutrinosphere is higher than at the ν_e neutrinosphere. This implies $L_{\bar{\nu}_e} \gg L_{\nu_e}$, $\langle\epsilon_{\bar{\nu}_e}\rangle \gg \langle\epsilon_{\nu_e}\rangle$ and thus $Y_e^\nu \ll 0.5$. Using three-dimensional calculations of the merger of NSs with zero spin, Rosswog & Liebendörfer (2003) find that at ~15 ms following merger, $L_{\bar{\nu}_e} \simeq 3.5 L_{\nu_e}$, $\langle\epsilon_{\nu_e}\rangle \simeq 9$ and $\simeq 15$ MeV, which implies $Y_e^\nu \simeq 0.21$, consistent with our arguments (see also Surman et al. 2008). We conclude that when the disc is optically thick near r_*, a neutron-rich outflow is again the most likely outcome. The critical accretion rate at which $\tau_\nu(r_*) = 1$ is shown in Fig. 11 with a long dashed line for both $a = 0$ and 0.9.

Once the disc becomes optically thin near r_*, the difference between the ν_e and $\bar{\nu}_e$ spectra is much less pronounced. This occurs because (1) the neutrinos and antineutrinos originate from regions with the same temperature; (2) any net lepton flux out of the disc must remain modest (i.e. $L_{\nu_e}/\langle\epsilon_{\nu_e}\rangle \simeq L_{\bar{\nu}_e}/\langle\epsilon_{\bar{\nu}_e}\rangle$) and (3) the difference between the e^- and e^+ capture cross-sections for $kT \gg \Delta - m_e c^2$ is small. Taking $\langle\epsilon_{\nu_e}\rangle \sim \langle\epsilon_{\nu_e}\rangle \gg \Delta$, equation (31) shows that $Y_e^\nu \simeq 0.5$, a value in the range required to produce ^{56}Ni (which we discuss further in Section 5.4). Indeed, M08b used the steady-state, optically thin α-disc calculations of Chen & Beloborodov (2007) to calculate the neutrino radiation fields carefully, and showed that $Y_e^\nu \gtrsim 0.5$ over the majority of the disc (see their fig. 1). Although the precise spectra extracted from an α-disc calculation should be taken with caution, the conclusion that the ν_e and $\bar{\nu}_e$ spectra are similar for optically thin accretion (and $Y_e^\nu \simeq 0.5$) is probably robust.

Fig. 11 illustrates that under most conditions the outflows from hyperaccreting discs are neutron rich. Neutron-rich material ejected during the initial dynamical phase of compact object mergers has long been considered a promising source for producing Galactic r-process elements, whose precise astrophysical origin remains un-

certain (Lattimer & Schramm 1974; see, however, Qian 2000). In addition, Surman et al. (2008) find that winds driven from the remnant accretion disc at early times (when it is optically thick; upper left-hand quadrant of Fig. 11) are sufficiently neutron rich to produce successful r process. The outflows driven from the advective disc at late times, however, are unlikely to produce r-process elements, given their modest entropies and electron fractions of $Y_e \gtrsim 0.3$ (Figs 8 and 9). Instead, this modest Y_e material will be synthesized to form intermediate-mass neutron-rich isotopes (Hartmann, Woosley & El Eid 1985).

5.4 ^{56}Ni production and optical transients

As summarized in Fig. 11, most of the material in the outflow driven from a hyperaccreting disc will be neutron rich. Non-relativistic neutron-rich ejecta are difficult to detect because isotopes synthesized from low Y_e material are themselves very neutron rich and typically possess very short half-lives, on the order of seconds (e.g. Freiburghaus, Rosswog & Thielemann 1999). Thus, most of the radioactive energy is released at high optical depths and suffers severe adiabatic losses before the photons can diffusively escape. By contrast, ejecta with $Y_e^a \simeq 0.5$ are easier to detect because they can produce a significant quantity of ^{56}Ni (Hartmann et al. 1985), an isotope better suited to powering observable emission because its half-life $\simeq$6 d is comparable to the time-scale on which the outflow becomes optically thin. From Fig. 11 we see that outflows in a modest range of parameter space (middle/lower-left trapezoid) are capable of synthesizing ^{56}Ni. One caveat to this conclusion is that it only applies if the winds are primarily neutrino driven. If the outflow is instead magnetocentrifugally driven by a moderately strong open poloidal magnetic field (e.g. Levinson 2006; Xie, Huang & Lei 2007), then $Y_e^a \ll 0.5$ can result, even if $Y_e^\nu \simeq 0.5$ (M08b). In what follows we assume that the wind's are primarily neutrino driven.

Under this assumption, Fig. 12 shows the total ^{56}Ni mass, $M_{Ni} = (X_{Ni}/0.4)M_{Y_e=0.5}$, produced in outflows from hyperaccreting discs as a function of the disc's initial mass $M_{d,0}$ and radius $r_{d,0}$, where $M_{Y_e=0.5}$ is the total mass loss with $Y_e^a \simeq 0.5$ and X_{Ni} is the average ^{56}Ni mass fraction synthesized in the wind. We calculate $M_{Y_e=0.5}$ by integrating the neutrino-driven mass loss (equations 24 and 26) across the $Y_e^a \simeq 0.5$ region in Fig. 11, using $r_d(t)$ and $\dot{M}_d(t)$ from the disc evolution calculations described in Section 4.

Pruet et al. (2004) present calculations of X_{Ni} which are parametrized in terms of the asymptotic entropy S^a, mass-loss rate $\dot{M}_w$ and asymptotic velocity v^a of an outflow with $Y_e^a \simeq 0.51$. $M_{Y_e=0.5}$ is dominated by outflows from radii $\sim 3 \times 10^6$–10^7 cm when $\dot{M}_d \sim 0.1$–$1 M_\odot$ s^{-1} (corresponding to $L_{52} \sim$ few); equation (25) thus gives $S^a \sim 10$–$30 k_B$ baryon^{-1} for the ejecta with $Y_e^a \simeq 0.5$. Purely neutrino-driven winds achieve asymptotic velocities which are typically below the escape speed of the central object (e.g. Thompson, Burrows & Meyer 2001); thus, the asymptotic kinetic energy is most likely dominated by energy released during the formation of heavy elements. Because ~ 8 MeV baryon^{-1} is released in producing Fe-peak elements, we estimate that $v^a \simeq 0.1$–$0.15c$. Applying these wind parameters to fig. 3 of Pruet et al. (2004), we estimate that $X_{Ni} \sim 0.2$–0.5, thereby justifying our scaling for X_{Ni} in Fig. 12.

Fig. 12 shows that for large initial disc masses ($M_{d,0} \gtrsim 0.1 M_\odot$), the ejected Ni mass, $\sim 3 \times 10^{-4}$–$10^{-3} M_\odot$, can be appreciable. Discs with moderate initial radii $r_{d,0} \sim 10^7$ cm are optimal for producing ^{56}Ni because they are sufficiently large to contain the radius $r_\nu \sim 10^7$ cm and yet are sufficiently compact to have a large initial accretion rate, which maximizes the neutrino luminosity and thus

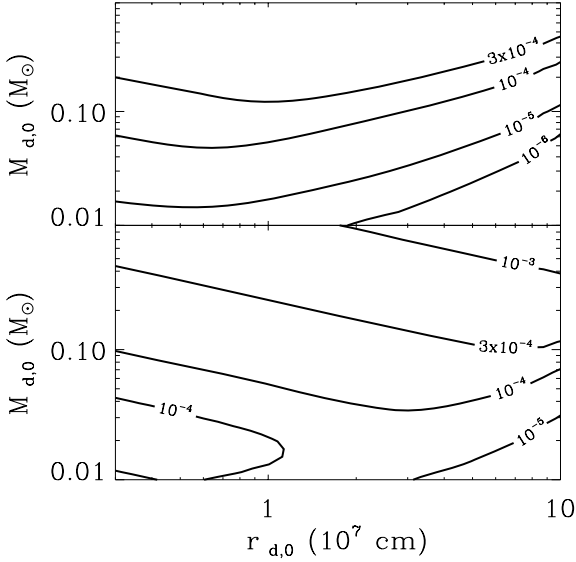**Figure 12.** Contours of total ^{56}Ni mass $M_{Ni} \equiv (X_{Ni}/0.4)M_{Y_e=0.5}$ (in units of $M_\odot$) produced in the neutrino-driven outflows as a function of the initial disc mass $M_{d,0}$ and initial ring radius $r_{d,0}$, where $M_{Y_e=0.5}$ is the total mass loss with $Y_e^a \simeq 0.5$ (based on the arguments in Fig. 11) and X_{Ni} is the average ^{56}Ni mass fraction synthesized in the wind. The upper and lower panels correspond to non-rotating ($a = 0$) and rapidly spinning ($a = 0.9$) BHs, respectively.

the neutrino-driven mass loss. Conveniently, initial disc parameters from many compact object merger simulations (see Section 2) are in the range required to produce $\sim 10^{-4}$–10^{-3} $M_\odot$ of Ni.

The decay of $M_{Ni} \sim 10^{-4}$–10^{-3} $M_\odot$ can reheat the (adiabatically cooled) ejecta sufficiently to produce detectable transient emission. In order to explore this possibility, we calculate the light curves of ejecta heated by Ni decay ('macronovae') using the method of Kulkarni (2005). This simplified one-zone model accounts for the fraction of the gamma-rays produced by the Ni decay which are absorbed by the expanding material (Colgate, Petschek & Kriese 1980) and assumes blackbody emission at the photosphere, neglecting Comptonization.

Fig. 13 shows the *V*- and *J*-band luminosities as a function of time since the merger for an outflow with Ni mass $M_{Ni} = 10^{-3}$ $M_\odot$ which is expanding at $v^a = 0.1c$. The *V*-band light-curve peaks earlier because the temperature at the photosphere decreases as the material expands. Somewhat after the peak in the light curves, recombination will decrease the opacity well below that considered here; thus our calculations are not quantitatively reliable at these times. The *total* mass M_{tot} ejected during the merger event, most of it neutron rich, is likely to be significantly larger than M_{Ni}; this provides additional opacity for the Ni-rich material. To explore the effect of this additional material on the detectability of the Ni decay, the light curves in Fig. 13 are shown for three values of M_{tot} : 10^{-3} $M_\odot$ (solid line), 10^{-2} $M_\odot$ (dotted line) and 10^{-1} $M_\odot$ (dashed line). As Fig. 13 shows, larger M_{tot}: (1) delays the time to peak emission (t_{peak} is roughly $\propto M_{tot}^{1/2}$); (2) increases the total fluence of the event by trapping a higher fraction of the gamma-ray emission and (3) increases the peak wavelength of the emission, pushing it into the near-infrared (IR) for large M_{tot}. We conclude that long wavelength ($\lambda \gtrsim \mu m$) observations at $t \sim 1$ d are the most promising for the detection of a Ni decay-powered macronova.

Hjorth et al. (2005) place an upper limit of $M_V > 27.5$ at $t = 3.9$ d on any emission associated with the short GRB 050509B (redshift
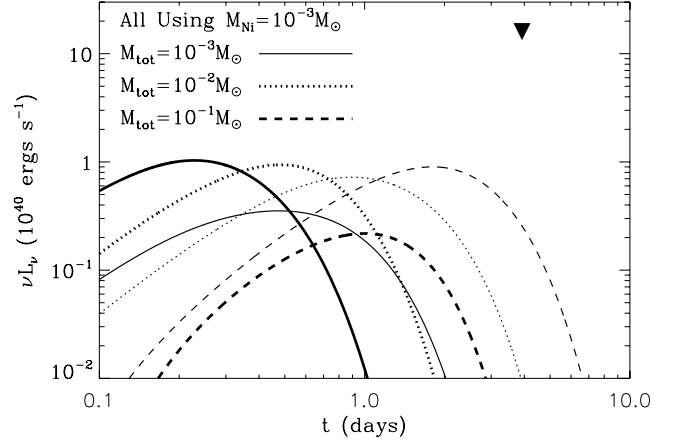

Figure 13. Luminosity of Ni decay-powered 'macronovae' as a function of time since merger for Ni mass $M_{Ni} = 10^{-3}$ $M_\odot$ and ejecta velocity $v^a = 0.1$ c. Light curves are shown for three values of the total ejected mass $M_{tot} = 10^{-3}$ $M_\odot$ (solid line), 10^{-2} $M_\odot$ (dotted line) and 10^{-1} $M_\odot$ (dashed line). The luminosities in *V* and *J* band (0.44 and 1.26 μm, respectively) are shown with thick and thin lines, respectively. The *V*-band upper limit on emission following GRB 050509B from Hjorth et al. (2005) is shown with a filled triangle.

$z \simeq 0.22$); we mark this constraint in Fig. 13 with an arrow. For $M_{tot} = 0.1$ $M_\odot$ this constrains the ejected Ni mass to be $M_{Ni} \lesssim 10^{-2}$ $M_\odot$ (see also Kulkarni 2005). As Fig. 12 illustrates, compact object mergers are very unlikely to produce this much Ni, so the absence of a detection thus far is unsurprising.

6 CONCLUSION AND DISCUSSION

We have calculated the time-dependent evolution of accretion discs formed from compact mergers, and the properties of their outflows. Since most of the disc mass resides at large radii, we approximate the disc as a ring at a given radius and calculate the dynamics and composition of the ring as a function of time. This ring model is calibrated to correctly reproduces the Green's function solution for a viscously spreading ring with viscosity $\nu \propto r^{1/2}$ (appropriate for a thick disc; see Appendix A). With this simplified model, we have studied the full parameter space of remnant accretion discs (different initial masses, compositions etc.) and can follow the viscous evolution for arbitrarily long time-scales.

The energetics of the ring at a given time can be described by one of three models: (1) optically thick to neutrinos and advective, (2) optically thin to neutrinos and geometrically thin and (3) optically thin to neutrinos and advective. A massive, compact disc (with a short initial viscous time $t_{visc,0}$; equation 5) will exhibit all three of these accretion phases, evolving from (1) to (3) as a function of time (Figs 1–4). Less massive discs, on the other hand, only pass through phases (2) and (3), or even just (3). Note that these phases refer to the energetics of the disc near the outer radius. At a given time, the disc may also undergo similar transitions as a function of radius; e.g. a disc that is advective at large radii will be neutrino cooled and geometrically thin inside the ignition radius r_{ign} (equation 19).

Neutrino-driven winds during the early-time optically thick and neutrino-cooled (thin disc) phases unbind so much mass that field lines connected to the disc cannot produce sufficiently relativistic material to power short-duration GRBs (Section 5.1 and Fig. 10). An alternative source for the relativistic material needed to produce short GRBs are nearly baryon-free magnetic field lines that thread

the BH's event horizon (e.g. McKinney 2005). In addition, when the inner disc becomes advective ($\dot{M}_d \lesssim 0.07\, \alpha_{0.1}^{5/3}$ M$_\odot$ s^{-1} for $a = 0$), conditions appear particularly suitable for the formation of relativistic jets (by analogy to X-ray binaries, which produce jets when making a similar transition; e.g. Remillard & McClintock 2006; see Lazzati et al. 2008 for a similar argument in the context of long-duration GRBs).

Once the disc has transitioned to a late-time advective phase (phase 3 above), the properties of the disc become well described by self-similar solutions. Ignoring for the moment outflows from the disc, these solutions are $r_d \propto t^{2/3}$, $M_d \propto t^{-1/3}$ and $\dot{M}_d \propto t^{-4/3}$. Power-law variations in the disc properties are a generic feature of a viscously evolving disc that conserves total angular momentum. These scalings are not, however, likely to be applicable in practice because outflows during the advective phase unbind most of the remaining material (Sections 4.1 and 5.2). Energy produced by fusion to He and heavier elements also contributes to driving an outflow (Figs 3 and 4). Such outflows remove a significant fraction of the angular momentum of the disc. This leads to a much more rapid decrease in the disc mass and accretion rate at late times (Appendix B3 and Fig. 6). Significant accretion on to the central black hole will thus only last for a few viscous times after the onset of the advective phase.

At the outer edge of the disc, the transition from a neutrino-cooled thin disc to the late-time advective phase occurs at a time $t_{thick} \sim 0.1\, \alpha_{0.1}^{-23/17} (J_{49}/2)^{9/17}$ s (equation 20). The rapid decrease in $\dot{M}_d$ after the onset of the advective phase implies that the inner disc becomes advective at a similar time (Section 5.2 and Fig. 6). Quantitatively, we find that for powerful winds with $p = 1$ (see equation B8), the inner disc becomes advective at $t \sim 0.2$, 5 and 100 s, for $\alpha = 0.1$, 0.01 and 0.001, respectively (for our fiducial model with an initial mass of 0.1 M$_\odot$ and an initial radius of $\simeq 3 \times 10^7$ cm). Thus, for $\alpha \sim 10^{-3}$, the time-scale for the inner disc to become advective is comparable to the onset of observed flaring at ~ 30 s in some short GRBs (e.g. Berger et al. 2005). Given the slow decline in disc mass with time before t_{thick}, there is ample accretion energy available in the disc at this point to power the observed flaring. However, there is observational evidence for $\alpha \sim 0.1$ in a number of astrophysical discs (King et al. 2007); we thus doubt that t_{thick} is large enough to coincide with the onset of observed flaring. Instead t_{thick} is likely to be ~ 0.1–1 s, comparable to the duration of the short GRB itself. In this case, the rapid decrease in the disc mass and accretion rate in the advective phase imply that the remnant accretion disc alone does not contain sufficient mass at ~ 30 s to power the observed late-time activity from short GRBs, nor is there any physical reason to expect a sudden change in the disc or jet properties at this time.

A more likely source of late-time flaring in compact object merger models is a continued inflow of mass at late times, such as is produced by the infalling tidal tail found in Lee & Ramirez-Ruiz's (2007) NS–NS merger simulations (see also Rosswog 2007). Similarly, the BH–NS merger simulations of Faber et al. (2006a,b) show that ~ 0.03 M$_\odot$ of material is ejected into highly eccentric orbits during the merger, which returns to the BH on a time-scale $\gtrsim 1$ s. However, final conclusions regarding the quantity and ubiquity of late-time fall-back from NS–NS and BH–NS mergers must await full-GR simulations which include BH spin and realistic EOSs.

The second major focus of this paper has been on the composition of the accretion disc and its outflows as a function of time. For initial disc properties expected in compact object mergers (Section 2), the disc typically comes into β equilibrium given the high temperatures and densities at small radii. As material spreads to larger radii, however, the composition of the disc freezes out before it becomes advective at late times; at freeze-out the disc is modestly neutron rich, with an electron fraction $Y_e \approx 0.3$ (Section 4.2 and Fig. 9). This neutron-rich material – $\sim 10^{-2}$ M$_\odot$ for typical initial disc parameters – is blown away once the disc enters the advective phase at $\sim t_{thick}$. These outflows are particularly interesting given the low Solar system abundance of material produced in NSE at $Y_e \sim 0.3$ (Hartmann et al. 1985). In a separate paper, we will study this nucleosynthesis and its implications in more detail.

Although outflows from compact object merger accretion discs are neutron rich in most circumstances, neutrino-driven winds from radii $\simeq 10^6$–10^7 cm at accretion rates $\dot{M}_d \sim 0.03$–1 M$_\odot$ s^{-1} have electron fractions $Y_e \simeq 0.5$, precisely that required to synthesize significant amounts of ^{56}Ni (Fig. 11). We have calculated the total Ni mass ejected by compact object merger discs as a function of their initial mass and radius (Section 5.4 and Fig. 12). Discs with initial masses $\gtrsim 0.1$ M$_\odot$ can produce up to $\sim 10^{-3}$ M$_\odot$ of ^{56}Ni. The radioactive decay of this Ni as the outflow expands to large radii will produce an optical and infrared transient peaking ~ 0.5–2 d after the merger, with a peak flux of $\nu L_\nu \simeq 10^{40}$ erg s^{-1} (Fig. 13). Because the Ni mass is likely to be a small fraction of the total mass of the ejecta (most of which is neutron rich), this transient is best detected at ~ 1 μm. As Fig. 13 shows, current observational limits on SN-like transients coincident with short GRBs are about a factor of ~ 10 above our predictions. However, somewhat deeper limits from a moderately closer burst could start to put interesting constraints on short GRB progenitors. It is also possible that the decay of some neutron-rich isotopes could heat the outflow and contribute to the late-time thermal emission (although most such isotopes have very short half-lives). This possibility should be investigated in future calculations using a nuclear reaction network.

Although we have focused on short GRBs throughout this paper, many of our results can be applied more broadly. For example, long-duration GRBs show late-time activity and flaring similar to that seen in short GRBs (e.g. Falcone et al. 2007). For the reasons described above, this activity is probably produced by a continued inflow of mass at late times (fallback from the stellar progenitor's envelope) rather than solely by the viscous evolution of the small-scale disc. As a final application of our results, we note that the AIC of a white dwarf to a neutron star is expected to produce a compact disc of ~ 0.1–0.5 M$_\odot$ outside the newly formed neutron star's surface (Dessart et al. 2006). The calculations presented here describe the evolution of this remnant disc, with the one caveat that the composition of the disc in the AIC context may be strongly affected by neutrino irradiation from the newly formed neutron star.

REFERENCES

Barthelmy S. D. et al., 2005, Nat, 438, 994
Barzilay Y., Levinson A., 2008, New Astron., 13, 386
Baumgarte T. W., Shapiro S. L., Shibata M., 2000, ApJ, 528, L29
Beloborodov A. M., 2003a, ApJ, 585, L19
Beloborodov A. M., 2003b, ApJ, 588, 931

Berger E. et al., 2005, Nat, 438, 988
Bildsten L., Cutler C., 1992, ApJ, 400, 175
Blandford R. D., Begelman M. C., 1999, MNRAS, 303, L1
Bloom J. S. et al., 2006, ApJ, 638, 354
Campana S. et al., 2006, A&A, 454, 113
Chen W. X., Beloborodov A. M., 2007, ApJ, 657, 383
Colgate S. A., Petschek A. G., Kriese J. T., 1980, ApJ, 237, L81
Dai Z. G., Wang X.-Y., Wu X.-F., Zang B., 2006, Sci, 311, 1127
Daigne F., Mochkovitch R., 2002, A&A, 388, 189
Derishev E. V., Kocharovsky V. V., Kocharovsky V. V., 1999, ApJ, 521, 640
Dessart L., Burrows A., Ott C. D., Livne E., Yoon S.-C., Langer N., 2006, ApJ, 644, 1063
Dessart L., Burrows A., Livne E., Ott C. D., 2008a, ApJ, 673, L43
Dessart L., Ott C., Burrows A., Rosswog S., Livne E., 2008b, preprint (arXiv:0806.4380)
DiMatteo T., Perna R., Narayan R., 2002, ApJ, 579, 706
Duez M. D., Liu Y. T., Shapiro S. L., Stephens B. C., 2004, Phys. Rev. D, 69, 104030
Duez M. D., Liu Y. T., Shapiro S. L., Shibata M., Stephens B. C., 2006, Phys. Rev. D, 73, 104015
Eichler D., Livio M., Piran T., Schramm D. N., 1989, Nat, 340, 126
Faber J. A., Baumgarte T.-W., Shapiro S.-L., Taniguchi K., Rasio F. A., 2006a, Phys. Rev. D, 73, 4012
Faber J. A., Baumgarte T.-W., Shapiro S.-L., Taniguchi K., 2006b, ApJ, 641, L93
Falcone A. D. et al., 2007, ApJ, 671, 1921
Ferrero P. et al., 2007, AJ, 134, 2118
Fishbone L. G., 1973, ApJ, 185, 43
Fox D. B. et al., 2005, Nat, 437, 845
Frank J., King A. R., Raine D. J., 2002, Accretion Power in Astrophysics, 3rd edn. Cambridge Univ. Press, Cambridge
Freiburghaus C., Rosswog S., Thielemann F.-K., 1999, ApJ, 525, L121
Galama T. J. et al., 1998, Nat, 385, 670
Gehrels N. et al., 2005, Nat, 437, 851
Haensel P., Zdunik J. L., 1990a, A&A, 227, 431
Haensel P., Zdunik J. L., 1990b, A&A, 229, 117
Hartmann D., Woosley S. E., El Eid M. F., 1985, ApJ, 297, 837
Hawley J. F., Balbus S. A., 2002, ApJ, 573, 738
Hjorth J. et al., 2003, Nat, 423, 847
Hjorth J. et al., 2005, ApJ, 630, L117
Janiuk A., Perna R., DiMatteo T., Czerny B., 2004, MNRAS, 355, 950
Janka H.-Th., Eberl T., Ruffert M., Fryer C. L., 1999, ApJ, 527, L39
King A. R., O'Brien P. T., Goad M. R., Osborne J., Page K., 2005, ApJ, 630, L113
King A. R., Pringle J. E., Livio M., 2007, MNRAS, 376, 1740
Kluźniak W., Lee W. H., 1998, ApJ, 494, L53
Kohri K., Mineshige S., 2002, ApJ, 577, 311
Kopal Z., 1959, Close Binary Systems. Chapman & Hall, London
Krolik J. H., Hirose S., Blaes O., 2007, ApJ, 664, 1045
Kulkarni S. R., 2005, preprint (astro-ph/0510256)
Kumar P., Narayan R., Johnson J. L., 2008, MNRAS, 388, 1729
Lai D., Rasio F. A., Shapiro S. L., 1994, ApJ, 423, 344
La Parola V. et al., 2006, A&A, 454, 753
Lattimer J. M., Schramm D. N., 1974, ApJ, 192, L145
Lazzati D., Ramirez-Ruiz E., Ghisellini G., 2001, A&A, 379, L39
Lazzati D., Perna R., Begelman M. C., 2008, MNRAS, 388, L15
Lee W. H., Kluźniak W., 1995, Acta Astron., 45, 705
Lee W. H., Kluźniak W., 1998, ApJ, 526, 178
Lee W. H., Kluźniak W., 1999, MNRAS, 308, 780
Lee W., Ramirez-Ruiz E., 2007, New J. Phys., 9, 17
Lee W. H., Ramirez-Ruiz E., Page D., 2004, ApJ, 608, L5
Lee W. H., Ramirez-Ruiz E., Page D., 2005, ApJ, 632, 421
Lemoine M., 2002, A&A, 390, L31
Levinson A., 2006, ApJ, 648, 510
Li L.-X., Paczyński B., 1998, ApJ, 507, L59
McKinney J. C., 2005, preprint (astro-ph/0506368)
Metzger B. D., Thompson T. A., Quataert E., 2008, ApJ, 676, 1130 (M08b)
Montanari E., Frontera F., Guidorzi C., Rapisarda M., 2005, ApJ, 625, L17

Morrison I. A., Baumgarte T. W., Shapiro S. L., 2004, ApJ, 610, 941
Nakar E., 2007, Phys. Rep., 442, 166
Narayan R., Piran T., Shemi A., 1991, ApJ, 379, L17
Narayan R., Piran T., Kumar P., 2001, ApJ, 557, 949
Oechslin R., Janka H.-Th., 2006, MNRAS, 368, 1489
Paczyński B., 1986, ApJ, 308, L43
Paczyński B., 1991, Acta Astron., 41, 257
Perna R., Armitage P. J., Zhang B., 2005, ApJ, 636, L29
Pethick C. J., Ravenhall D. G., 1995, Annu. Rev. Nucl. Part. Sci., 45, 429
Piro A. L., Pfahl E., 2007, ApJ, 658, 1173
Popham R., Woosley S. E., Fryer C. L., 1999, ApJ, 518, 356
Price D. J., Rosswog S., 2006, Sci, 312, 719
Proga D., Begelman M. C., 2003, ApJ, 592, 767
Proga D., Zhang B., 2006, MNRAS, 370, L61
Pruet J., Thompson T. A., Hoffman R. D., 2004, ApJ, 606, 1006
Qian Y.-Z., 2000, ApJ, 534, L67
Qian Y.-Z., Woosley S. E., 1996, ApJ, 471, 331 (QW96)
Qian Y.-Z., Fuller G. M., Mathews G. J., Mayle R. W., Wilson J. R., Woosley S. E., 1993, Phys. Rev. Lett., 71, 1965
Rasio F. A., Shapiro S. L., 1994, ApJ, 432, 242
Rasio F. A., Faber J., Kobayashi S., Laguna P., 2005, Proc. JGRG14 Yukawa Institute for Theoretical Physics, preprint (astro-ph/0503007)
Remillard R. A., McClintock J. E., 2006, ARA&A, 44, 49
Rossi E. M., Beloborodov A. M., Rees M. J., 2006, MNRAS, 369, 1797
Rosswog S., 2007, MNRAS, 376, L48
Rosswog S., Liebendörfer M., 2003, MNRAS, 342, 673
Rosswog S., Speith R., Wynn G. A., 2004, MNRAS, 351, 1121
Ruffert M., Janka H.-Th., 1999, A&A, 344, 573
Ruffert M., Janka H.-Th., 2001, A&A, 380, 544
Ruffert M., Janka H.-Th., Schäfer G., 1996, A&A, 311, 532
Ruffert M., Janka H.-Th., Takahashi K., Schäfer G., 1997, A&A, 319, 122
Setiawan S., Ruffert M., Janka H.-Th., 2004, MNRAS, 352, 753
Setiawan S., Ruffert M., Janka H.-Th., 2006, A&A, 458, 553
Shakura N. I., Sunyaev R. A., 1973, A&A, 24, 337
Shapiro S. L., Teukolsky S. A., 1983, Black Holes, White Dwarfs, and Neutron Stars: The Physics of Compact Objects. Wiley, New York
Shibata M., Taniguchi K., 2006, Phys. Rev. D, 73, 064027
Shibata M., Taniguchi K., Uryū K., 2005, Phys. Rev. D, 71, 084021
Shibata M., Duez M. D., Liu Y.-T., Shapiro S. L., Stephens B., 2006, Phys. Rev. Lett., 96, 031102
Soderberg A. M. et al., 2006, ApJ, 650, 261
Stanek K. Z. et al., 2003, ApJ, 591, L17
Stone J. M., Pringle J. E., 2001, MNRAS, 322, 461
Surman R., McLaughlin G. C., Hix W. R., 2006, ApJ, 643, 1057
Surman R., McLaughlin G. C., Ruffert M., Janka H.-Th., Hix W. R., 2008, ApJ, 679, L117
Thompson T. A., Burrows A., Meyer B. S., 2001, ApJ, 562, 887
Thompson T. A., Chang P., Quataert E., 2004, ApJ, 611, 380
Uryū K., Eriguchi Y., 1999, MNRAS, 303, 329
Villasenor J. S. et al., 2005, Nat, 437, 855
Woosley S. E., Baron E., 1992, ApJ, 391, 228
Xie Y., Huang C.-Y., Lei W.-H., 2007, Chin. J. Astron. Astrophys., 7, 685

APPENDIX A: CALIBRATION OF THE RING MODEL

The surface density Σ of an axisymmetric disc in a Keplerian potential with constant total angular momentum evolves according to a diffusion equation (e.g. Frank, King & Raine 2002):

$$\frac{\partial \Sigma}{\partial t} = \frac{3}{r} \frac{\partial}{\partial r} \left[r^{1/2} \frac{\partial}{\partial r} (\nu \Sigma r^{1/2}) \right], \tag{A1}$$

where ν is the kinematic viscosity. Assuming that ν depends only on radius as a power law, viz: $\nu = \nu_0 (r/R_0)^n$, equation (A1) is linear and, for an initial surface density distribution $\Sigma(r, t = 0) = (M_0/2\pi R_0)\delta(r - R_0)$ which is narrowly peaked about the radius R_0,

the solution (for $n < 2$) is given by

$$\Sigma(r, t)$$
$$= \frac{M_0(1 - n/2)}{\pi R_0^2 x^{(n+1/4)}\tau} \exp\left[\frac{-(1 + x^{2-n})}{\tau}\right] I_{1/|4-2n|}\left(\frac{2x^{1-n/2}}{\tau}\right), \quad (A2)$$

where M_0 is the initial disc mass, $x \equiv r/R_0$, $\tau \equiv t[12\nu_0(1 - n/2)^2/R_0^2]$ and I_m is a modified Bessel function of order m. For small argument $y \ll 1$, $I_m(y)$ takes the asymptotic form $I_m \simeq (y/2)^m/\Gamma(m + 1)$, where Γ is the Gamma function; thus, for late times or small radii such that $\tau \gg 2x^{1-n/2}$, equation (A2) reduces to

$$\Sigma(r, t)|_{\tau \gg 2x^{1-n/2}}$$
$$= \frac{M_0}{\pi R_0^2} \frac{(1 - n/2)}{\Gamma[(5 - 2n)/(4 - 2n)]} \frac{1}{\tau^{[(5-2n)/(4-2n)]}x^n} \exp\left[\frac{-(1 + x^{2-n})}{\tau}\right]. \quad (A3)$$

Most of the mass in the disc is located near the radius where the local mass $M_d \propto \Sigma r^2$ peaks; using equation (A3), at late times this radius is found to be $r_{peak} = R_0\tau^{1/(2-n)}$. Hence, equation (A3) becomes valid near r_{peak} for $\tau \gg 1$.

The constant A, which relates the total disc mass at late times from the exact solution of equation (A1) to the mass defined by $\pi\Sigma(r_{peak})r_{peak}^2$, can be calculated from equation (A3) to be

$$A(\tau \gg 1) \equiv \frac{\int_0^\infty 2\pi\Sigma r \, dr}{\pi\Sigma(r_{peak})r_{peak}^2}\bigg|_{\tau \gg 1} = \frac{2e}{2 - n}. \quad (A4)$$

Similarly, the constant B, which relates the total disc angular momentum at late times from the exact solution to that estimated by $\pi\Sigma r_{peak}^2 (GMr_{peak})^{1/2}$, is given by

$$B(\tau \gg 1) \equiv \frac{\int_0^\infty 2\pi\Sigma r^{3/2} \, dr}{\pi\Sigma(r_{peak})r_{peak}^{5/2}}\bigg|_{\tau \gg 1} = \frac{2e}{2 - n}\Gamma\left(\frac{5 - 2n}{4 - 2n}\right). \quad (A5)$$

From mass continuity, the radial velocity is given by

$$v_r = \frac{-3}{\Sigma r^{1/2}}\frac{\partial}{\partial r}\left(\nu\Sigma r^{1/2}\right) = \frac{-3\nu_0}{R_0}\frac{1}{\Sigma x^{1/2}}\frac{\partial}{\partial x}\left(\Sigma x^{n+1/2}\right), \quad (A6)$$

which, using equation (A3), gives the accretion rate at small radii

$$\dot{M}_{in} = -2\pi\Sigma r v_r|_{\tau \gg 2x^{1-n/2}}$$
$$= \frac{M_0}{R_0^2/\nu_0} \frac{3(1 - n/2)}{\Gamma[(5 - 2n)/(4 - 2n)]} \exp(-1/\tau)\tau^{-[(5-2n)/(4-2n)]}. \quad (A7)$$

Equation (A7) is easily checked by noting that $\int_0^\infty \dot{M}_{in}dt = M_0$, which shows that the entire initial disc eventually accretes on to the central object. In Section 3.1 we introduced the following prescription for evolving the disc mass:

$$\dot{M}_d = \frac{fM_d}{t_{visc}}, \quad (A8)$$

where, in terms of the viscosity prescription adopted above, $t_{visc} = r_d^2/\nu = t_{visc,0}(r_d/R_0)^{2-n}$ and $t_{visc,0} \equiv R_0^2/\nu_0$ is the initial viscous time. Assuming that the total disc angular momentum remains constant, $J \propto M_d r_d^{1/2} = M_0 R_0^{1/2}$, the solution to equation (A8) is given by

$$M_d(t) = M_0[1 + (4 - 2n)f(t/t_{visc,0})]^{-1/(4-2n)}. \quad (A9)$$

In our evolutionary calculations we set f so that the accretion rate from the exact solution to equation (A1) ($\dot{M}_{in}$; equation A7) matches the solution to equation (A8) at late times (i.e. in the self-similar limit). This requires

$$f = 3(1 - n/2)\Gamma[(5 - 2n)/(4 - 2n)]^{4-2n}. \quad (A10)$$
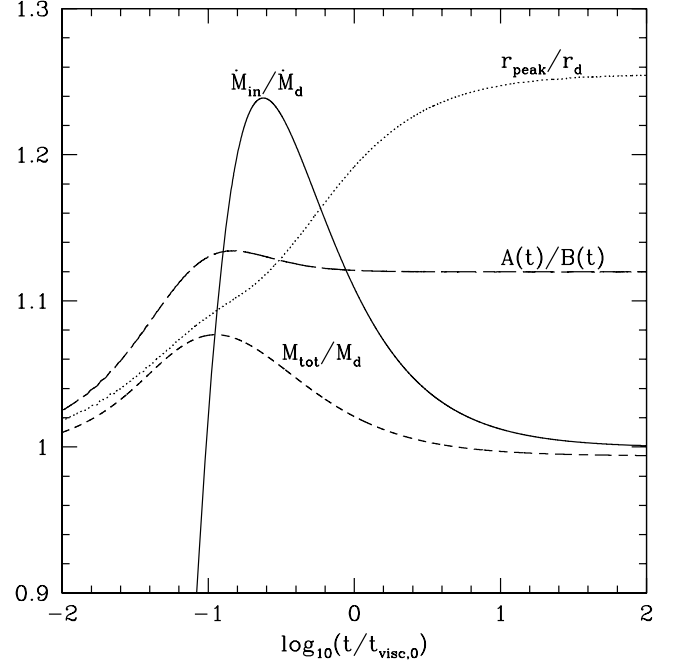

Figure A1. Comparison of the accretion rate (solid), disc mass (short dashed) and disc radius (where the local disc mass peaks; dotted) as calculated from our simplified ring model to that derived from the exact solution of the diffusion equation for a δ function initial mass distribution (equation A2); we assume $\nu \propto r^{1/2}$, as applies for a thick disc. The parameter $f \simeq 1.6$ (equation A10) adopted in our model is chosen to ensure that the accretion rates match at late times (i.e. $\dot{M}_{in}/\dot{M}_d \to 1$). Also shown is the ratio $A(t)/B(t)$ (equations A4 and A5), a measure of the relative distribution of mass and angular momentum, which asymptotes to $\Gamma[(5 - 2n)/(4 - 2n)] \simeq 1.12$ at late times.

For an advection-dominated disc, $\nu = \alpha c_s H \propto \Omega R^2 \propto r^{1/2}$; thus, $n = 1/2$, $f \simeq 1.602$, $A \simeq 3.62$ and $B \simeq 3.23$. For a neutrino-cooled, optically thin disc which is dominated by gas pressure, $T \propto r^{-3/10}$ and $\nu \propto r^{6/5}$; thus, $n = 6/5$, $f \simeq 1.01$, $A \simeq 6.80$ and $B \simeq 6.09$.

In Fig. A1 we show $\dot{M}_{in}/\dot{M}_d$ as a function of $t/t_{visc,0}$ for $n = 1/2$ in order to compare the disc evolution derived from the exact solution of equation (A1) to that calculated from our simplified model. Fig. A1 also shows the ratio of the total disc mass $M_{tot} \equiv \int_0^\infty 2\pi\Sigma r dr$ calculated from equation (A2) to the disc mass M_d (equation A9) of the simplified model, as well as the ratio of r_{peak} (the radius where Σr^2 peaks, using equation A2 for Σ) to the radius determined by angular momentum conservation: $r_d = R_0(M_d/M_0)^2$. Fig. A1 shows that, although the accretion rate in the two models differ at very early times (the initially narrowly concentrated ring takes a short period of time to spread to small radii), they approach one another to $\lesssim 20$ per cent by $t \gtrsim 0.1 t_{visc,0}$. Likewise, the disc mass and radii from the exact solution and simplified model are quite similar at all times.

The numerical values for A and B given in equations (A4) and (A5) and employed in our calculations apply only to the mass and angular momentum distribution in the disc at late times ($\tau \gg 1$). Initially, the disc is entirely concentrated at a single radius and $A(t = 0) = B(t = 0) = 1$; thus, $A(t)$ and $B(t)$ evolve significantly from early times until the disc enters the self-similar limit and so one might worry that the early-time description of the disc's evolution depends sensitively on the initial mass distribution. Our model only assumes, however, that the *ratio* $A(t)/B(t)$ remains constant, which

is a good approximation. To illustrate this, Fig. A1 shows $A(t)/B(t)$ calculated from the exact solution (equation A2) for $n = 1/2$. Note that $A(t)/B(t)$ increases from unity to its asymptotic value $A/B = \Gamma[(5 - 2n)/(4 - 2n)]$, which is $\simeq 1.12$ for $n = 1/2$.

APPENDIX B: ANALYTIC SELF-SIMILAR SOLUTIONS

The late-time evolution of our disc calculations asymptote to power laws that are well approximated by analytic self-similar solutions. We derive these here to aid in interpreting our numerical results. Presentation is divided between neutrino-cooled, thin-disc solutions and late-time advective solutions. One could just as well derive analogous results for discs that are optically thick to neutrinos. We forgo this here since the initial viscous time is always sufficiently long that these solutions are never applicable to our numerical results. We conclude by presenting self-similar solutions for advective discs with substantial mass loss, since these differ significantly from the solutions without mass loss.

B1 Neutrino-cooled, thin-disc solutions

In the neutrino-cooled, thin-disc limit, the cooling is dominated by Urca, and the pressure is given by ideal gas. Combining local energy balance and continuity, $\dot{M}_d = fA\pi\nu\Sigma$, allows us to solve for the temperature and column density as functions of radius. We substitute these into the angular momentum equation, $B(GMr_d)^{1/2}\pi r_d^2\Sigma = J_d$, to solve for M_d as a function of $\dot{M}_d$ and J_d. We then assume the solutions have a self-similar form of $M_d \propto t^{-\beta}$, so that $\dot{M}_d = -dM_d/dt = \beta M_d/t$. In this way we solve for $\beta = 5/8$, $\dot{M}_d(t)$, and subsequently any other variable of interest. The results are

$$M_d = 1.3 \times 10^{-2} f_{1.6}^{-5/8} \left(\frac{A_{3.6}}{B_{3.2}}\right) \alpha_{0.1}^{-3/4} M_3^{-1/4} \left(\frac{J_{49}}{2}\right) t^{-5/8} \, \mathrm{M_\odot}, \quad \text{(B1)}$$

$$\dot{M}_d = 2.7 \times 10^{-2} f_{1.6}^{-5/8} \left(\frac{A_{3.6}}{B_{3.2}}\right) \alpha_{0.1}^{-3/4} M_3^{-1/4} \left(\frac{J_{49}}{2}\right) t^{-13/8} \, \mathrm{M_\odot \, s^{-1}} \quad \text{(B2)}$$

and

$$r_d = 4.1 \times 10^8 f_{1.6}^{5/4} \alpha_{0.1}^{3/2} M_3^{-1/2} t^{5/4} \, \mathrm{cm}, \quad \text{(B3)}$$

where $f_{1.6} = f/1.6$, $A_{3.6} = A/3.6$, $B_{3.2} = B/3.2$ and t is measured in seconds, and the prefactors have been scaled to match our numerical results. The first thing to notice is that both M_d and $\dot{M}_d$ are rather insensitive to the choice of f as long as it is near unity, and A and B only appear as a ratio, which is also nearly unity. This provides confidence in using this parametrization, and these specific values for the corresponding parameters, when the disc is not well-described by $n = 1/2$. This analysis also demonstrates the relative dependence on α. In Fig. B1 we compare these scaling (dotted lines) with the numerical calculations. This shows that these solutions are only applicable for a short time. At times when $t < t_{\mathrm{visc}}$ the evolution is much flatter and is dominated by initial conditions. At later times the disc becomes advective and the solutions of the next section apply.

B2 Late-time advective solutions

In this limit, self-similar solutions can be found in an analogous way. The viscous energy release is carried by advection with the
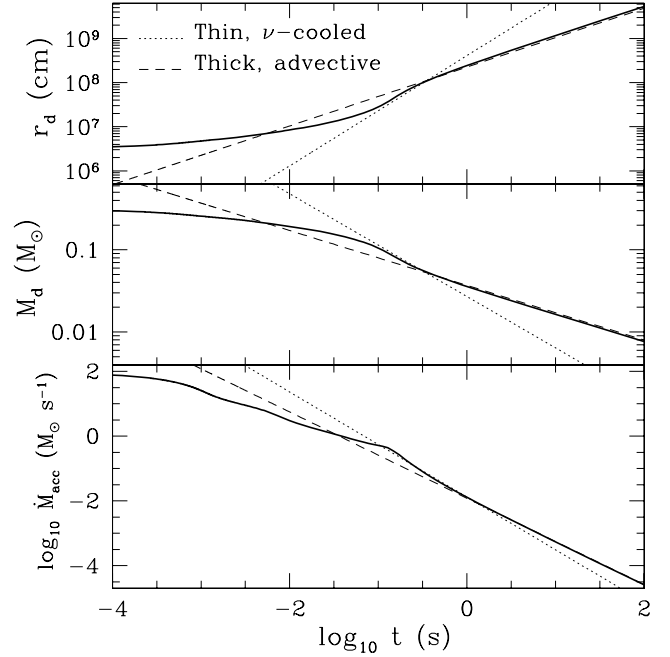

Figure B1. Comparison of the numerical disc solutions (solid lines) with the analytic solutions for the thin, neutrino-cooled (dotted lines) and thick, advective limits (dashed lines). The numerical solution is the $0.3\,\mathrm{M_\odot}$ disc from Fig. 1.

internal energy dominated by relativistic particles, so that

$$\frac{9}{8fA\pi}\Omega^2\dot{M} = V_r\frac{H}{r}\frac{11}{6}aT^4. \quad \text{(B4)}$$

Combining this with mass continuity, gives the column depth as a function of radius, $\Sigma(r) = (16/9A\pi\alpha)(\dot{M}/r^2\Omega)$. We then use this relation with $B(GMr_d)^{1/2}M_d = J_d$ and $\dot{M}_d = \beta M_d/t$, to find $\beta = 1/3$ and the self-similar solutions

$$M_d = 3.7 \times 10^{-2} \left(\frac{A_{3.6}}{B_{3.2}}\right) \alpha_{0.1}^{-1/3} M_3^{-2/3} \left(\frac{J_{49}}{2}\right) t^{-1/3} \, \mathrm{M_\odot}, \quad \text{(B5)}$$

$$\dot{M}_d = 1.2 \times 10^{-2} \left(\frac{A_{3.6}}{B_{3.2}}\right) \alpha_{0.1}^{-1/3} M_3^{-2/3} \left(\frac{J_{49}}{2}\right) t^{-4/3} \, \mathrm{M_\odot s^{-1}} \quad \text{(B6)}$$

and

$$r_d = 2.3 \times 10^8 \alpha_{0.1}^{2/3} M_3^{1/3} t^{2/3} \, \mathrm{cm}. \quad \text{(B7)}$$

These advective results are even more insensitive to A, B and f than the thin-disc results. Equations (B5)–(B7) are plotted in Fig. B1 as dashed lines. The numerical calculations follow these solutions very closely for times later than t_{thick} (given by equation 20).

Equations (B5)–(B7) can also be derived ignoring equation (B4), but assuming that the scaleheight is fixed at $H/r \simeq 0.6$. This introduces the additional dependencies $M_d \propto (H/r)^{-2/3}$, $\dot{M}_d \propto (H/r)^{-2/3}$ and $r_d \propto (H/r)^{4/3}$, but gives nearly identical prefactors.

B3 Advective solutions with mass loss

In Section 5.2 we described how advective discs are likely to lose a substantial fraction of their mass to viscously driven outflows. Because the outflow removes angular momentum as well – at least the specific angular momentum of the mass that is lost – the disc need not expand as rapidly to large radii. In addition, the disc mass and accretion rate decrease much more rapidly at late times than in

the self-similar solutions described in the previous subsection. To quantify this effect, we follow Blandford & Begelman (1999) and assume that only a fraction $\sim (r_*/r_d)^p$ of the available material is accreted on to the central BH. The remainder is lost to an outflow. Thus the outflow rate at any time is given by

$$\dot{M}_{out} = \left[1 - \left(\frac{r_*}{r_d} \right)^p \right] \frac{f M_d}{t_{visc}}. \tag{B8}$$

We further assume that the angular momentum loss rate from the disc is given by

$$\dot{J} = -C \dot{M}_{out} (GMr_d)^{1/2}, \tag{B9}$$

where C is a constant that depends on the torque exerted by the outflowing mass on the remaining disc. If the outflow produces no net torque, an assumption that appears at least qualitatively consistent with the relatively small-scale magnetic fields seen in global MHD disc simulations (e.g. Stone & Pringle 2001), then the angular momentum loss is only that due to the specific angular momentum of the outflow, and (Kumar, Narayan & Johnson 2008)

$$C = \frac{2p}{2p+1}. \tag{B10}$$

We solve equations (6), (7), (B8) and (B9), assuming $A/B = 1$ and $\nu \propto r^{1/2}$ (as appropriate for a thick disc). The solution depends on the relative magnitude of $1 - C$ and $C(r_*/r_d)^p$. For $C(r_*/r_d)^p \ll 1 - C$, which is true at nearly all times if equation (B10) is applicable, then

$$r_d \simeq r_{d,0} \left[1 + 3f(1-C) \left(\frac{t}{t_{visc,0}} \right) \right]^{2/3}, \tag{B11}$$

$$M_d \simeq M_{d,0} \left[1 + 3f(1-C) \left(\frac{t}{t_{visc,0}} \right) \right]^{-1/[3(1-C)]} \tag{B12}$$

and

$$\dot{M}_{in} \simeq f \frac{M_{d,0}}{t_{visc,0}} \left(\frac{r_*}{r_{d,0}} \right)^p$$
$$\times \left[1 + 3f(1-C) \left(\frac{t}{t_{visc,0}} \right) \right]^{-[1+3(1+2p/3)(1-C)]/[3(1-C)]} \tag{B13}$$

Note that if $p = C = 0$ (i.e. no mass or angular momentum loss), then these self-similar solutions reduce to those of the previous subsection. However, for the case $p = 1$ consistent with a number of global advective disc simulations (e.g. Hawley & Balbus 2002), and in the absence of a net torque on the disc, $C = 2/3$ and these solutions correspond to $r_d \propto t^{2/3}$, $M_d \propto t^{-1}$ and $\dot{M}_{in} \propto t^{-8/3}$ (see also Fig. 6). This shows that the disc mass and accretion rate decrease subsantially more rapidly in time than in the absence of an outflow, while the disc expands outward at roughly the same rate. If there is a net torque on the disc such that $C \simeq 1$, then equations (B11)–(B13) are not applicable. Instead, for $C(r_*/r_d)^p \gg 1 - C$, the solution is given by (for $p \neq 0$ and $t \gg t_{visc,0}$)

$$r_d(t) \simeq \left[(3 + 2p) f r_*^p r_{d,0}^{1.5} \right]^{1/(1.5+p)} \left(\frac{t}{t_{visc,0}} \right)^{1/(1.5+p)} \tag{B14}$$

and

$$M_d(t) \simeq M_{d,0} \exp[-D(t/t_{visc,0})^{p/(1.5+p)}], \tag{B15}$$

where

$$D = \left[\frac{1.5 + p}{p(3+2p)^{1.5/(1.5+p)}} \right] \left[\frac{f r_{d,0}^{1.5}}{(f r_*^p r_{d,0}^{1.5})^{1.5/(1.5+p)}} \right]. \tag{B16}$$

For $p = 1$ and for $r_{d,0} \sim r_*$, these solutions become $r_d(t) \sim r_{d,0}(t/t_{visc,0})^{2/5}$ and $M_d(t) \sim M_{d,0} \exp[-1.15(t/t_{visc,0})^{2/5}]$. The radius of the disc thus increases significantly more slowly, and the mass of the disc decreases much more rapidly, than in the self-similar solutions without mass loss.

The numerical solutions including mass-loss during the advective phase shown in Section 4.1 (Fig. 6) assume that equation (B10) is applicable and are indeed well described by the self-similar solutions given in equations (B11)–(B13) at late times.

This paper has been typeset from a TeX/LaTeX file prepared by the author.